nature communications

Article

https://doi.org/10.1038/s41467-025-58239-x

Structural basis for psilocybin biosynthesis

Received: 17 July 2024

Accepted: 17 March 2025

Chunyan Meng[1,2,9], Wenting Guo[1,9], Chuan Xiao[1,9], Yan Wen[1,3,9], Xudong Zhu[1], Qingrong Zhang[4], Yuxuan Liang[4], Hongwei Li[1], Sha Xu[5], Yuntan Qiu[1,10] ✉, Haitao Chen[4,10] ✉, Wei-Jye Lin[1,6,7,8,10] ✉ & Baixing Wu[1,2,10] ✉

Psilocybin shows significant therapeutic potential for psilocybin-assisted psychotherapy in addressing various psychiatric conditions. The biosynthetic approach promises rapid and efficient production of psilocybin. Understanding the enzymes that contribute to the biosynthesis of psilocybin can enhance its production process. In this study, we elucidate the crystal structures of L-tryptophan-specific decarboxylase PsiD in both its apo and tryptamine-bound states, the 4-hydroxytryptamine kinase PsiK bound to its substrate, and several forms of the methyltransferase PsiM in either apo or substrate-bound forms derived from the psychedelic mushroom. Structure-based evaluations reveal the mechanisms of self-cleavage and self-inhibition in PsiD, along with the sequential catalytic steps from 4-hydroxytryptamine to the final compound, psilocybin. Additionally, we showcase the antidepressant properties of biosynthetic intermediates of psilocybin on female mice experiencing depression-like behaviors induced by sub-chronic variable stress. Our studies establish a structural basis for the future biosynthetic production of psilocybin using these enzymes and emphasize the clinical potential of norbaeocystin.

More than one billion people globally are believed to suffer from mental disorders, such as depression, bipolar disorder, schizophrenia, and others[1]. Over the past decade, the therapeutic potential of psychedelics for treating these disorders has drawn considerable attention, with more than ten completed clinical trials, particularly in the field of psychiatry[2]. One of the serotonergic hallucinogens, psilocybin (4-phosphoryloxy-N,N-dimethyltryptamine), has been proposed to possess medical potential for drug-assisted psychotherapy in treating psychiatric disorders[3–10]. Psilocybin is an indoleamine hallucinogen and a secondary metabolite produced by hundreds of mushroom species in the *Psilocybe* genus, which are distributed globally[4,11–14]. For centuries, mushrooms have been used in religious ceremonies by indigenous societies in South and Central America[9,15]. Psilocybin was first chemically characterized and crystallized from the dried *Psilocybe mexicana* mushroom by Albert Hofmann, who subsequently elucidated the structure and method of chemical synthesis of psilocybin[4,11,12]. When digested by humans, psilocybin is rapidly dephosphorylated to the main pharmacologically active substance, psilocin (4-hydroxy-N, N-dimethyltryptamine), by alkaline phosphatase in the liver[3,16] and nonspecific esterase in the intestinal mucosa[17]. Psilocin serves as a ligand and partial agonist of the 5-hydroxytryptamine (5-HT) receptors in humans, thereby profoundly impacting human perception and consciousness[4,18,19]. Psilocin's agonist activity at the 5-HT_{2A} receptor is generally considered necessary

---

[1]Guangdong Provincial Key Laboratory of Malignant Tumor Epigenetics and Gene Regulation, Guangdong-Hong Kong Joint Laboratory for RNA Medicine, Medical Research Center, Sun Yat-Sen Memorial Hospital, Sun Yat-Sen University, Guangzhou, China. [2]Institute of Drug Discovery, Guangzhou Institutes of Biomedicine and Health (GIBH), Chinese Academy of Sciences (CAS), Guangzhou, China. [3]Breast Tumor Center, Sun Yat-Sen Memorial Hospital, Sun Yat-Sen University, Guangzhou, China. [4]School of Public Health (Shenzhen), Sun Yat-Sen University, Shenzhen, China. [5]State Key Laboratory of Oncology in South China, Guangdong Provincial Clinical Research Center for Cancer, Sun Yat-Sen University Cancer Center, Guangzhou, China. [6]Brain Research Center, Sun Yat-Sen Memorial Hospital, Sun Yat-Sen University, Guangzhou, China. [7]Nanhai Translational Innovation Center of Precision Immunology, Sun Yat-Sen Memorial Hospital, Foshan, China. [8]Guangdong Provincial Key Laboratory of Brain Function and Disease, Zhongshan School of Medicine, Sun Yat-Sen University, Guangzhou, China. [9]These authors contributed equally: Chunyan Meng, Wenting Guo, Chuan Xiao, Yan Wen. [10]These authors jointly supervised this work: Yuntan Qiu, Haitao Chen, Wei-Jye Lin, Baixing Wu. ✉e-mail: qiuyt8@mail2.sysu.edu.cn; chenht56@mail.sysu.edu.cn; linwj26@mail.sysu.edu.cn; wu_baixing@gibh.ac.cn

for psychedelic activity to produce a “mystical-like” hallucinatory effect due to induced frontal hyper-frontality[20], which in turn mediates its antidepressant and anti-anxiety effects[21].

The increasing rate of global mood and anxiety disorders and the therapeutic potential will spur the demand for psilocybin. However, the extraction of psilocybin from naturally growing or cultivated mushrooms is not economically viable for drug research and development[17]. Therefore, chemical methods for synthesizing psilocybin have been developed to improve the yield of psilocybin to kilogram-scale with single (or few) dose regimes[22,23]. Alternatively, psilocybin could also be produced through synthetic biological methods based on the inspiring work that identified the genes encoding the enzymes for psilocybin biosynthesis in *Psilocybe* and other genera[24,25]. The metabolic pathway was shown to involve the activity of four enzymes, including PsiD, PsiH, PsiK, and PsiM[22,24,26] (Fig. 1a). Characterization of these enzymes confirmed that L-tryptophan acts as the raw material in the biosynthetic pathway. PsiD functions as the decarboxylase that catalyzes L-tryptophan into tryptamine, which can subsequently be catalyzed by the indole-4-monooxygenase PsiH to produce 4-hydroxytryptamine. Meanwhile, it has also been validated that PsiD could directly convert 4-hydroxy-L-tryptophan to 4-hydroxytryptamine[24]. Following these processes, another critical enzyme, PsiK, further catalyzes 4-hydroxytryptamine to norbaeocystin by adding a phosphate group to the 4-hydroxyl position of 4-hydroxytryptamine using the co-substrate ATP[24]. The terminal amino group of norbaeocystin will be methylated by the PsiM protein to form baeocystin and psilocybin, step by step, using the cofactor S-adenosylmethionine (SAM)[24]. Per the elucidation of the biosynthesis pathway[24], bioengineering has led to the production of psilocybin in the filamentous fungi *Aspergillus nidulans*[27], *Escherichia coli*[28], and *Saccharomyces cerevisiae*[29]. Studies have also reported a scalable hybrid synthetic/biocatalytic route to produce psilocybin by replacing the phosphorylation step with the PsiK kinase[22] and a biocatalytic route to synthesize 6-methyl-norbaeocysin, 6-methyl-baeocysin, and 6-methyl-psilocybin from 4-hydroxy-6-methyl-L-tryptophan. In that study, the recombinantly expressed PsiD, PsiK, and PsiM enzymes were used to achieve the processing steps[26]. However, although these enzymes have been biochemically characterized according to the in-silico models[22,26,30], the experimental structures of these enzymes are still valuable in promoting the development of engineering more productive pathways for psilocybin biosynthesis.

Here, we first determine the structures of PsiD in its apo and substrate-bound forms. Based on the structural analysis, we propose potential mechanisms for the self-cleavage and decarboxylation reactions of PsiD. Additionally, we uncover the self-inhibition mechanism of the PsiD proenzyme and demonstrate that deleting the N-terminal region significantly increases its decarboxylase activity. Next, we solve the structure of PsiK in complex with the cofactors and tryptamine substrate. We uncover the cofactors and substrate-binding properties of PsiK and identify the key residues for the phosphorylation reaction. We then determine the structures of PsiM in its apo- and different substrate-bound forms, revealing its stepwise methylation mechanism. Finally, we evaluate the biological effects of the intermediate products of psilocybin in sub-chronic variable stress-induced depression-like behaviors in mice. Our structural and biochemical characterization of the enzymes involved in psilocybin biosynthesis, combined with the behavioral experiments, will shed light on optimizing the synthetic biological methods for psilocybin production and the combined administration of psilocybin with the other intermediate products.

Results

The PsiD proenzyme undergoes self-cleavage

To uncover the catalytic mechanism of PsiD, we expressed the full-length PsiD (1–439) protein from *Psilocybe cubensis* and determined its crystal structure using the molecular replacement method with the model predicted by AlphaFold2 (Fig. 1b, Supplementary Table 1, Supplementary Fig. 1a)[24,31]. There are six PsiD molecules in the asymmetric unit that have similar conformations, with an RMSD of about 0.2–0.3 Å over equivalent backbone atoms (Supplementary Fig. 1b). However, the density of the N-terminal ~53–57 residues could not be modeled in all these molecules (Supplementary Fig. 1a–h); therefore, we selected one of the PsiD molecules containing residues 53–438 (hereafter named apo-PsiD) for further analysis (Supplementary Fig. 1c).

Consistent with previous observations in studies of the *E. coli* phosphatidylserine decarboxylases (PSDs)[32–34], which indicate that the proenzyme undergoes a self-cleavage reaction and can be divided at a conserved “LGST” motif by a canonical serine protease mechanism[35,36], the PsiD enzyme exhibited self-cleavage between a “GGSS” (G401-G402-S403-S404) motif, leaving a pyruvoyl prosthetic group within the N-terminal of the α-chain, which was then named Pvl403, and a β-chain containing a Gly402 terminus (Fig. 1c, d). The production of the active Pvl403 group was confirmed by our mass spectra results (Supplementary Fig. 2a). The self-cleavage reaction mechanism of the PsiD protein can be deduced from previous studies of the PSDs, the biochemical characterization and the in-silico modeling structure of *P. cubensis* PsiD[30,34]. Firstly, the peptide bond between Gly402 and Ser403 undergoes serinolysis attacked by the side chain hydroxyl group of Ser403, forming an ester bond between the two amino acids. Then, an α, β-elimination reaction will break the linkage between the two residues, and the β-subunit will be released, leaving a dehydroalanine at the N-terminus of the α-subunit; a water molecule will further attack the double bond of the dehydroalanine intermediate to yield the α-hydroxyl alanyl residue, which will subsequently form the mature pyruvoyl moiety by releasing ammonia[34,37,38] (Fig. 1e).

The overall structure of PsiD

The α and β chains of each PsiD protomer in the asymmetric unit form a globular fold that consists of 16 α-helices and 13 β-strands (Fig. 1d, Supplementary Fig. 2b). The Gly402 at the C-terminus of the β chain is positioned ~11 Å away from the pyruvoyl group, as predicted by the published AlphaFold2 model (Fig. 1f)[30]. This conformational change results in the exposure of the pyruvoyl group for further catalytic reactions. The putative active site is surrounded by four structural elements mainly composed of hydrophobic residues, including the Loop 1 region (aa. 108–120), the Loop 2 region (aa. 290–297), the Loop 3 region (aa. 324–341), and the Loop 4 region (aa. 371–377) (Fig. 1g, h).

Further analysis revealed that the PsiD molecules might form a homodimer that adopts central symmetry with an extensive dimer interface (Supplementary Fig. 3a). Half of the dimer interface was then selected to show these contacts (Supplementary Fig. 3b). The Asp251, Glu281, Gln253, Ser254, Lys261, and Asp256 from one molecule formed various hydrogen bonds with Asp71, Arg137, Arg135, Gln136, Asn139, and Thr134 from another molecule, either directly or mediated by water molecules. Meanwhile, Thr257, Val259, and Phe260 from one molecule had hydrophobic contacts with Thr134, Ile348, Phe130, Pro321, and Tyr344 from another molecule. The residues involved in dimer formation are all located within the β-chain (Supplementary Fig. 3c). Following our observations, Arg135 and Gln136 were mutated (R135A/Q136A) to assess the in-solution status of PsiD through gel filtration, with wildtype PsiD and S403A serving as controls (Supplementary Fig. 3d). However, our evaluation indicated that both wildtype PsiD and the PsiD mutants predominantly exist as monomers, with only a minor fraction displaying the homodimer form. Additionally, the R135A/Q136A mutation did not significantly alter the in-solution status of PsiD. These results suggested that the PsiD protein mainly exists as a monomer in the solution state, while some also form a homodimer state.

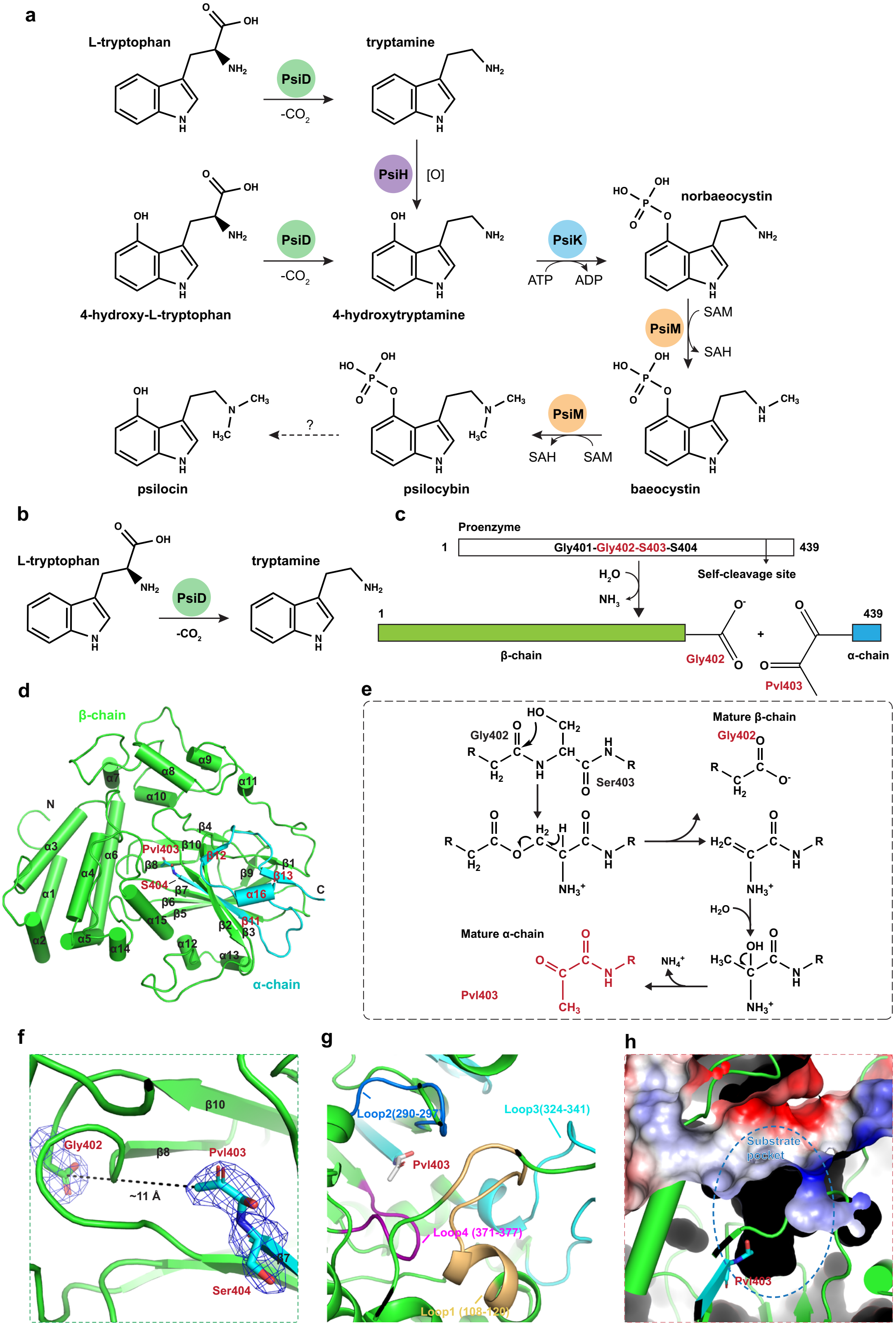

Fig. 1 | Structure of L-tryptophan decarboxylase PsiD. **a** Enzymatic synthesis pathway of psilocybin in *P. cubensis*. The reaction scheme was redrawn from a previous study[24]. **b** Schematic representation of the catabolic substrate and product of the PsiD protein. **c** The schematic depicts the self-cleavage mechanism of PsiD from the proenzyme to the mature enzyme. **d** The overall structure of the PsiD protein. The α-chain is colored cyan, and the β-chain is colored green. The pyruvoyl group is shown as sticks. **e** The potential reaction scheme for the self-cleavage of the PsiD proenzyme. **f** The distance between the C-terminal of the β-chain Gly402 and the N-terminal Pvl403 of the α-chain after self-cleavage. The residues G402 and Pvl403 are shown as sticks. The |Fo|-|Fc| map is contoured at 3.0 σ (colored blue). **g** The four loop regions responsible for pocket formation are colored yellow, blue, cyan, and purple, respectively. **h** The electrostatic surface representation of the substrate-binding pocket. The pocket region containing Pvl403 is indicated by a blue circle.

Structure of the Schiff-base intermediate of PsiD with L-tryptophan

To further investigate substrate recognition and the catalytic mechanism, we determined the structure of PsiD complexed with the substrate L-tryptophan through co-crystallization (Supplementary Table 1). Hereafter, we refer to this structure as PsiD-Trp. There are also six PsiD molecules in the crystallographic asymmetric unit, showing minor differences (Supplementary Fig. 4a–g). Thus, we selected one of them to compare with the apo-PsiD structure (Fig. 2a, Supplementary Fig. 4b). Structural comparisons between the PsiD-Trp complex and the apo-PsiD revealed no significant conformational changes in the PsiD structure upon substrate binding, as demonstrated by the RMSD of about 0.24 Å between these two structures over equivalent backbone atoms (Fig. 2a).

In accordance with previous observations that the pyruvoyl prosthetic group forms a Schiff-base intermediate with the primary amine of the substrate during catalysis[32–34], the Schiff-base intermediate between Pvl403 and the amino group of L-tryptophan was captured in our PsiD-Trp structure (Fig. 2b). Meanwhile, the carboxyl group of L-tryptophan could not be modeled, indicating that the structure of PsiD in complex with L-tryptophan presents a covalently bound intermediate state with tryptamine. In this structure of the PsiD-Trp complex, the methyl group of Pvl403 was hydrophobically anchored by the side chains of Phe398, His296, and Leu290. The covalent amide was hydrogen-bonded to the main chain of Leu290. The only hydrophilic group in the indole ring of tryptamine forms hydrogen bonds with the side chain of Thr374 and the main chain of Met373. The indole ring was enclosed by Phe289, Val292, Leu339, Leu112, Tyr338, Tyr117, Pro114, Met373, Thr374, and Ile376, thereby stabilizing the intermediate product (Fig. 2b, c). These residues were almost all within the pocket-composing loops (Fig. 2d). Structure superposition suggested minor deviations in the catalytic pocket between the apo-PsiD and the PsiD-Trp complex. Only two residues had slight conformational differences between these structures: His296 and Val292, which are closer to the indole ring when PsiD binds to the intermediate product (Fig. 2e).

Decarboxylase activity assay

To examine the functional roles of the residues involved in substrate binding, we made several PsiD mutants and measured their decarboxylase activities using the thin-layer chromatography (TLC) method. Before doing that, we first tested the catalytic activity of the wildtype PsiD using a TLC experiment and validated the catalytic product through mass spectrometry analysis (Fig. 2f, g, Supplementary Fig. 5a). Based on these results, we then performed the TLC assays to test the activity of the PsiD mutants (Fig. 2h, i, Supplementary Fig. 5b). In vitro decarboxylation activity assays revealed that the L112A and F289A mutations did not decrease the decarboxylase activity of PsiD but enhanced its catalytic activity. These observations may be attributed to weak hydrophobic interactions with the substrate; in contrast, Y117A reduced the activity. On the other hand, L290A almost completely lost its decarboxylase activity for L-tryptophan, indicating the key role of Leu290 in producing and stabilizing the pyruvoyl group. The Tyr338, necessary for hydrophobic contact with the substrate, also shows slightly increased activity when mutated to alanine. The Thr374, which forms a hydrogen bond with the L-tryptophan molecule, did not dramatically impact the catalytic ability of PsiD; as a negative control, the mutants of His296 and Ser403, which are indicated to be essential for the self-cleavage reactions[30,39], abolished both self-cleavage and L-tryptophan decarboxylase activity when replaced with alanine (H296A and S403A) (Fig. 2g–j, Supplementary Fig. 5b), while the Gly402 mutant (G402A), located at the terminus of the β-chain and not involved in covalent bond formation, showed similar activity to the L-tryptophan substrate as the wildtype did (Fig. 2g–j, Supplementary Fig. 5b). The results mentioned above validated the roles of the residues we identified in the catalytic pocket for decarboxylase activity. Unfortunately, although we tried to purify the other mutations involved in substrate binding and pyruvoyl group formation, such as F398A, M373A, and P114G, these mutants were not stable enough to be purified.

The N-terminal of PsiD revealed a self-inhibition mechanism

Based on the above enzymatic assays, a confusing observation was that the wildtype PsiD protein exhibited insufficient catalytic activity toward the substrate, leaving a certain amount of L-tryptophan not fully reacted (Fig. 2f, Supplementary Fig. 5a, c). To figure out why the recombinant full-length PsiD did not have strong enough activity, we performed the decarboxylase assay using TLC methods with gradient pH values (Tris pH 7.4-9.0) according to our protein purification and crystallization conditions. However, the different pH values showed a minor impact on the catalytic activity of the PsiD protein under our experimental conditions (Supplementary Fig. 5d). In contrast, previous studies suggested that the optimal condition for PsiD activity occurred in sodium phosphate buffer (pH 6.6) and between 33 and 36 °C[30]. These distinctions may explain the capture of the covalent-bound tryptamine product state in our structure of the PsiD-Trp complex.

To explore whether other factors exist that cause the insufficient catalytic activity of PsiD, we reanalyzed its N-terminal region (aa. 1–55), which remained invisible in both the structures of apo-PsiD and the PsiD-Trp complex. A structure superposition between the AlphaFold2-predicted full-length PsiD and our PsiD-Trp structures showed that the N-terminal region might not impact the dimerization of the PsiD protein (Supplementary Fig. 6a, b). However, the N-terminal region contains three alpha-helices that lie on the surface of the solved part of the PsiD structure. Moreover, the first helix covers the substrate-binding pocket of PsiD, with a tryptophan (Trp27) residue inserted into the substrate-binding pocket, sharing the same set of residues for substrate recognition (Fig. 3a, b). These analyses strongly suggest a cryptic self-inhibition mechanism in the PsiD protein that inhibits the enzyme's activity. Therefore, we chose to construct two additional truncations, PsiD (aa. 50–439) and PsiD (aa. 30–439), as well as a W27A mutant of the full-length PsiD to test their catalytic activity. The S403A was selected as a negative control (Fig. 3c–f, Supplementary Fig. 7a–e). The TLC results revealed that the PsiD (1–439) W27A mutant, as well as the PsiD (30–439), showed significantly higher catalytic activities for the L-tryptophan substrate than the wildtype PsiD enzyme (Fig. 3c–e, Supplementary Fig. 7a–c). Furthermore, deleting the N-terminal 50 residues dramatically increased the catalytic activity of the PsiD protein for the L-tryptophan substrate (Fig. 3c, f, Supplementary Fig. 7d). Incubating these different constructs with L-tryptophan also validated these results; all the L-tryptophan substrate was converted to tryptamine in PsiD (1–439) W27A, PsiD (30–439), and PsiD (50–439), but not in the wildtype PsiD under the same conditions (Fig. 3g, Supplementary Fig. 7f, g). Accordingly, none of these truncations or the W27A impact the self-cleavage activity of PsiD (Fig. 3h).

We then co-crystallized PsiD (50–439) with L-tryptophan and successfully obtained the structure at a high resolution of 1.6 Å (Supplementary Table 1, Supplementary Fig. 8a). Structural comparison of the PsiD (50–439)-Trp complex revealed no significant differences from the PsiD-Trp complex (Supplementary Fig. 8b). However, in contrast to the tryptamine in the latter complex, which is presented in a covalently bound state, the former complex shows a pre-release state when superimposing the catalytic centers of these two structures (Fig. 3i, j). These results demonstrate that the PsiD enzyme has a self-inhibition mechanism through its N-terminal region, particularly the Trp27 residue, thereby regulating its activity. Deleting the N-terminal region will dramatically improve decarboxylation efficiency.

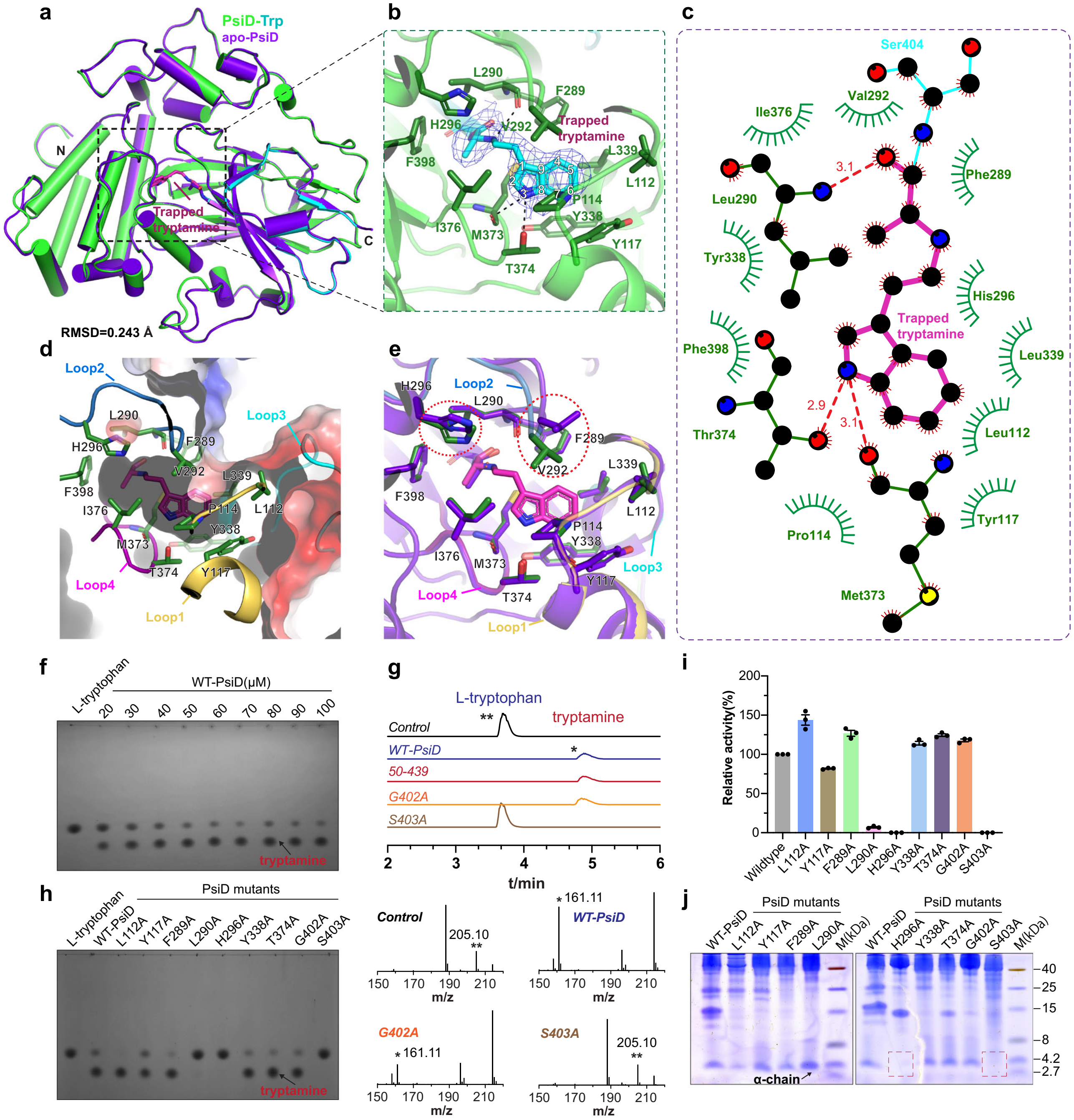

Fig. 2 | The substrate-binding properties of PsiD. a Structural superposition of the apo-PsiD protein and the PsiD-Trp complex. The trapped tryptamine is shown as sticks. **b** The substrate-binding status of the covalently bonded tryptamine by the pyruvoyl group of the PsiD α-chain. The |Fo|-|Fc| map is contoured at 3.0 σ (colored blue). **c** A LIGPLOT diagram listing critical contacts between tryptamine and the PsiD protein. **d** Surface representation of the pocket composed of the four loop regions enclosing the substrate. **e** The conformational changes of the two residues, His296 and Val292, between the apo-PsiD and substrate-binding statuses are indicated by red circles. **f** TLC experiment for testing the product of the decarboxylation reaction of PsiD to L-tryptophan. **g** Chromatographic analysis of activity assays to detect tryptamine formation by wildtype PsiD, G402A, and S403A. Control: chromatograms of the L-tryptophan reference with heat-inactivated PsiD protein. *: tryptamine; **: L-tryptophan. **h** The TLC results for testing the product of the decarboxylation reaction of PsiD mutants to L-tryptophan. All the TLC experiments are independently repeated three times. **i** Quantitative analysis of the TLC results for testing the product of the decarboxylation reaction of PsiD mutants to L-tryptophan. All data are presented as mean ± SEM. **j** SDS-PAGE results for determining the self-cleavage status of wildtype or mutated PsiD proteins. The experiments are independently repeated at least three times.

The working model and reaction scheme of PsiD

Searching for the structural homolog of PsiD using the Dali online server identified only one homologous protein, PSD, from *E. coli*[40]. Therefore, we compared the structures of *Ec*PSD and PsiD to elucidate their distinctions and similarities in substrate recognition. The detailed descriptions of the comparison results are provided in Supplementary Note 1 (Supplementary Figs. 9 and 10). Drawing from our structural studies, functional assays, and biochemical characterization from earlier research[30], along with the reaction scheme of *Ec*PSD[38], we proposed a working model and catalytic mechanism for the biosynthesis of tryptamine catalyzed by PsiD (Fig. 3k): (a) In the catalytically inactive state, the N-terminus of PsiD covers the surface region

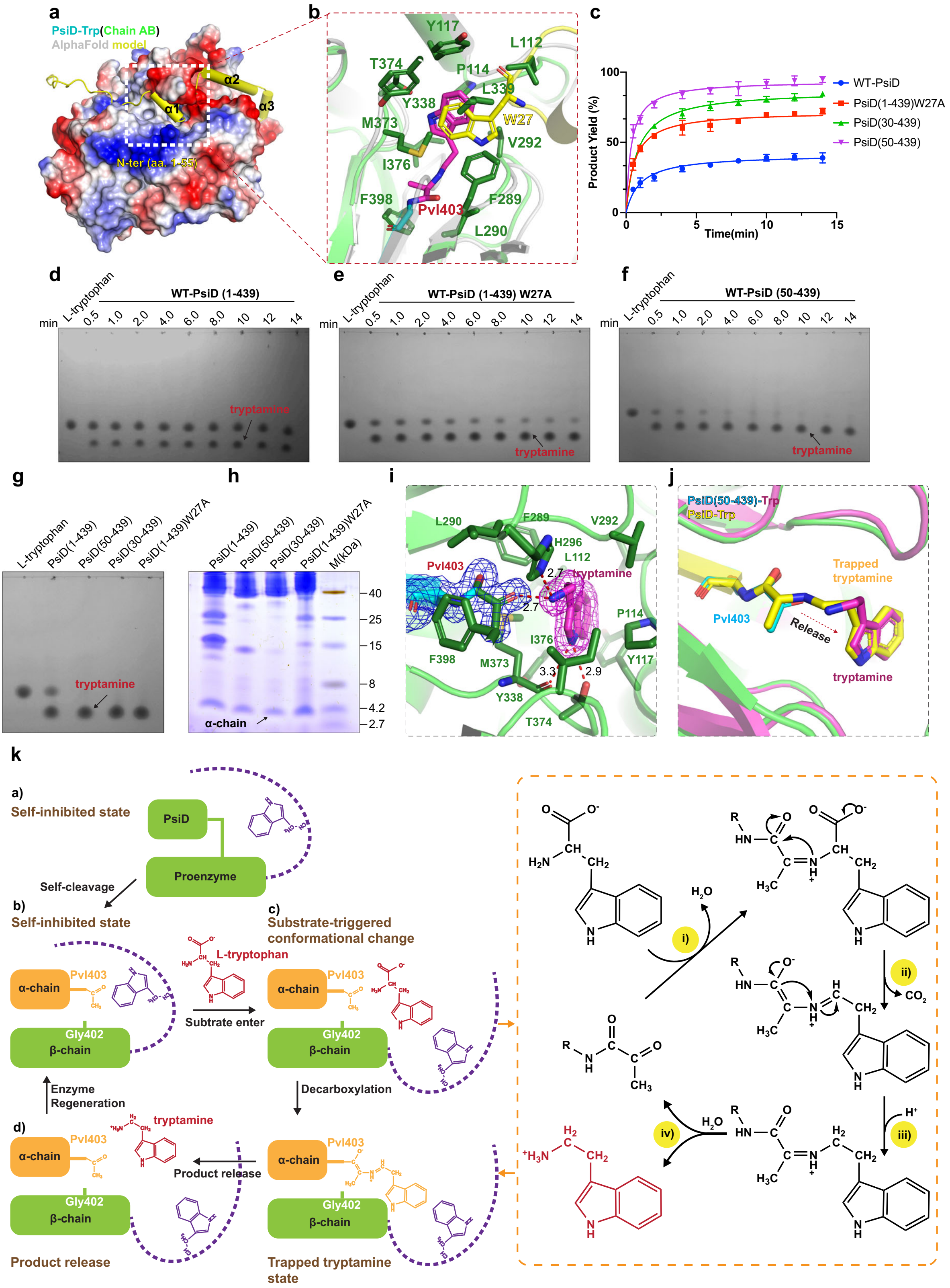

above the catalytic pocket with Trp27 inserted, leading to the self-inhibition of the PsiD enzyme; (b) Then, the PsiD proenzyme undergoes self-cleavage between Gly402 and Ser403, producing the mature enzyme with a catalytically active pyruvoyl prosthetic group (Pvl403) at the N-terminal of the α-chain; (c) During the catalytic process, the L-tryptophan substrate triggers conformational changes in the N-terminal, at least competing with the Trp27 residue to enter the catalytic center. The detailed catalytic reaction scheme can be deduced from the PSDs[34,38]: (i) First, the hydrophobic indole ring of L-tryptophan is attracted into the pocket and binds to the active site via a Schiff-base formed between the primary amine of L-tryptophan and the α-carbonyl carbon of Pvl403; (ii) The electron rearrangement favors decarboxylation, and the formation of an azomethine intermediate; (iii) Subsequent protonation generates another intermediate

Fig. 3 | The self-inhibition mechanism of PsiD. a Electrostatic surface representation of the PsiD-Trp structure overlaid with the AlphaFold2-predicted PsiD model. **b** Comparison of the substrate-binding states of the PsiD-Trp and the N-terminal inhibited state of the predicted PsiD model. **c** Quantitative results of the TLC experiment testing the catalytic activity of wildtype PsiD, PsiD (1–439) W27A, PsiD (30–439), and PsiD (50–439). All data are presented as mean ± SEM. All the TLC experiments are independently repeated three times. **d–g** The TLC experiment results for testing the catalytic activity of wildtype PsiD, PsiD (1–439) W27A, PsiD (30–439), and PsiD (50–439). **h** The SDS-PAGE results for determining the self-cleavage status of wildtype PsiD, PsiD (50–439), PsiD (30–439), and PsiD (1–439) W27A proteins. The results are independently repeated at least three times. **i** The tryptamine-bound state of the PsiD (50–439)-Trp complex. Tryptamine is colored purple, and the Pvl403 group is colored cyan. The |Fo|-|Fc| map is contoured at 3.0 σ (colored blue and purple). **j** The comparison of the covalently bound and pre-release states of the tryptamine substrate in the structures of PsiD-Trp and PsiD (50–439)-Trp complexes. The trapped tryptamine is colored yellow, and the pre-released tryptamine is colored purple. **k** The proposed reaction scheme of the PsiD enzyme.

product in Schiff-base linkage with the enzyme; (iv) The addition of a water molecule across the Schiff-base regenerates the pyruvoyl prosthetic group and liberates tryptamine from the active site; (d) Finally, the enzyme may regenerate to catalyze a new round of reactions.

The overall structure of PsiK

Next, to uncover the phosphorylation mechanism of PsiK, we solved the structure of the PsiK complex with the cofactor ADP and tryptamine, which were used to capture the substrate-bound state of PsiK (Fig. 1a, Supplementary Table 1)[24]. In addition, two Mg^{2+} ions derived from the crystallization conditions were observed alongside the phosphate groups of the ADP molecule (Fig. 4a). The PsiK molecule contains a β-strand-rich smaller N-lobe (aa. 1–118) and a larger helix-rich C-lobe (aa. 126–362), with a total of nine β-strands and twelve α-helices (Fig. 4a). The cofactor ADP and the substrate were located in a long cleft beneath the N-lobe, with two metal ions situated between the cofactor and substrate (Fig. 4b).

Searching the structure of homologous proteins of PsiK revealed that the PsiK enzyme structurally resembles protein kinase-like phosphotransferases[40], especially the 5-Methylthioribose (MTR) kinases from *A. thaliana* and *B. subtilis*, with Z-scores of 32.4 and 31.3, and C_α RMSD values of 2.8 Å and 3.1 Å, respectively[41,42] (Supplementary Fig. 11a, b). Nevertheless, PsiK shares only ~16% sequence identity with these two MTR kinases. Previous studies have uncovered four loop regions in these MTR kinases that play critical roles in ADP binding, divalent cation chelation, and substrate recognition, including a glycine-rich loop (G-loop) between β1 and β2, an HGD catalytic loop, an Mg^{2+} binding DXE motif, and a semi-conserved W-loop[41,42] (Supplementary Fig. 12). In our PsiK structure, there are four loop regions and a linker that correspond to these regions in the MTR kinases, playing a role in substrate and cofactor binding (Fig. 4c). Based on these analyses, we further inspected the cofactor binding, divalent cation chelation, and substrate recognition properties of the PsiK protein.

Cofactor binding and substrate recognition properties of PsiK

During the phosphorylation process, the co-substrate ATP donates the γ-phosphate group to the substrate and produces the ADP molecule. The ADP molecule in our structural complex is clamped in a cleft between two β-sheet regions composed of β1-β5 and β7-β8 from the two lobes of PsiK (Fig. 4d). The adenine ring of the ADP points to the linker region and resides in a relatively hydrophobic area. The N^1 and N^6 nitrogen atoms of the ADP are hydrogen-bonded to the amide nitrogen of Val120 and the main-chain carbonyl of Gln118, respectively (Fig. 4d). The N^3 position of adenine forms hydrogen bonds with Arg41 via a water molecule. In addition to these hydrogen interactions, the ADP base is enclosed by several hydrophobic residues, including Val120, Leu231, Pro103, Leu248, Met117, Leu31, and Ile55. The conserved Lys57 residue interacts with the α- and β-phosphoryl groups of ADP, and the main chain of Gly228 contacts both the α-phosphoryl group and the $O^{3'}$ position of the ribose group of ADP (Fig. 4e, Supplementary Fig. 12). Asn37 and Thr39 form hydrogen bonds to the β-phosphoryl group to anchor and coordinate the ADP, either directly or via a water molecule (Fig. 4e).

The two Mg^{2+} ions (M1 and M2), which assist in the binding of ADP and are essential for kinase activity, were observed forming hexa-coordination structures with water molecules, PsiK residues, and ADP phosphoryl groups (Fig. 4e). The M1 ion hexa-coordinates with the oxygen atoms of the α- and β-phosphoryl groups of ADP, the side chains of Asp249 and Asn229, and two water molecules named w1 and w2; M2 has a hexa-coordinate status with the side chains of Glu251 and Asp249, the oxygen atom from the β-phosphoryl group of ADP, and two water molecules named w3 and w4. Asp249 and Asp251 are part of the strictly conserved "DXE" motif on the loop between strands β8 and β9, while Asn229 is located in the Loop 3 region (Supplementary Fig. 12).

The tryptamine we used to capture the substrate-binding state is stabilized by a channel full of hydrophobic residues, including Phe35, Met63, Val36, Phe69, Ile71, Thr180, Leu252, Leu184, Trp316, and Phe319 (Fig. 4f). Among them, two phenylalanine residues, Phe35 and Phe319, adopt a bolt-like conformation to lock in the tryptamine (Fig. 4f, g). The indole ring of tryptamine is inserted into the pocket toward the Mg^{2+} ions, leaving the terminal amino group pointing toward the pocket entry (Fig. 4f–h). The C^4 position of the indole ring points to Asp224, with about 5 Å of distance separated by two water molecules, w5 and w6 (Fig. 4h). Modeling 4-hydroxytryptamine in the pocket revealed that it is somewhat far from the catalytic active residue Asp224 (Fig. 4i). Therefore, the captured tryptamine represents an inactive state of the enzyme. We speculate that when the phosphorylation reaction of PsiK occurs, the 4-hydroxytryptamine substrate moves closer to Asp224 and occupies the position of w5.

We then compared the differences and similarities between the PsiK protein and the plant MTK enzyme in cofactor binding, Mg^{2+} chelation, and substrate recognition to deduce the catalytic scheme of PsiK (Supplementary Fig. 13a, b). The detailed description can be found in Supplementary Note 2. The PsiK employs a general acid-base mechanism to achieve the phosphorylation process (Fig. 4j): when the substrate binds, Asp224 functions as a base, accepting a proton from the substrate's 4-hydroxyl group. This action initiates the in-line nucleophilic attack of the negatively charged oxygen on the γ-phosphate, resulting in a transient complex. Subsequently, the substrate's 4-hydroxyl group cleaves the γ-phosphate, which is stabilized by M2, causing the intermediate to split into the phosphorylated products and ADP. The product is then released from the catalytic center, while ADP exhibits a lower affinity for the binding pocket[43].

Conformational changes of PsiM during the stepwise methylation reaction

To illustrate the methylation steps from norbaeocystin to psilocybin, we have also solved six structures of PsiM alone and in various complexes with SAH, SAM, SAH-norbaeocystin, SAH-baeocystin, and SAH-psilocybin (Fig. 5a–f, Supplementary Figs. 14–19). However, our structures align with the recently published findings[44]. Therefore, detailed descriptions of our results are provided in Supplementary Notes 3. Even so, our results provide a clearer picture of the sequential conformational changes of PsiM during the methylation steps (Fig. 5g, h): (i) In the apo state, the region between Pro185 and Gly222 was dynamic and unstable in the absence of the cofactor and substrate;

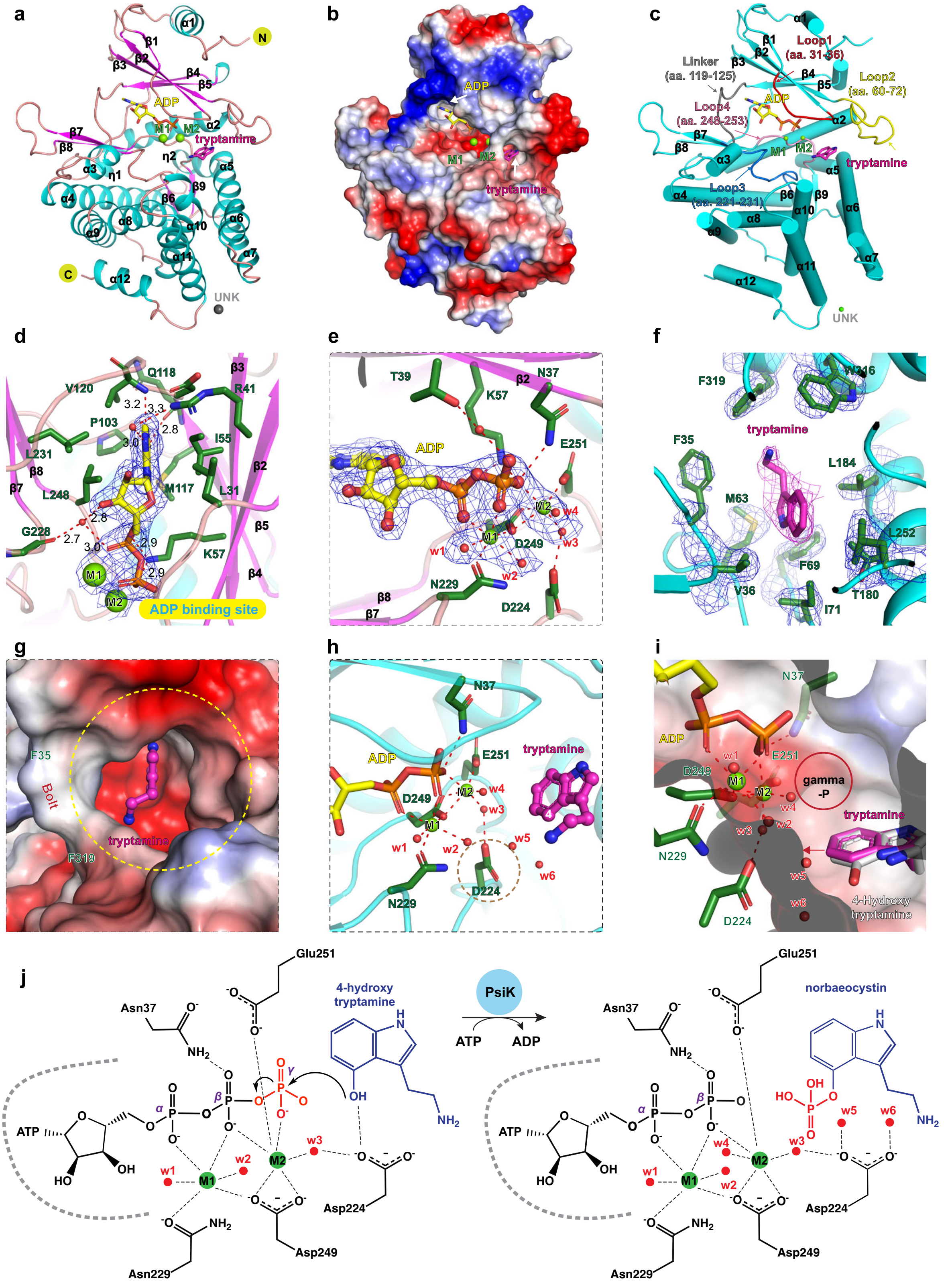

(ii) When SAM entered the cofactor binding site, Arg75 and Leu68 changed their conformations to stabilize SAM along with other residues. The region between Ala199 and Ser211 remained flexible without the substrate, while the regions of Pro185-Ala198 and Gly212-Gly222 were observed in the presence of the cofactor; (iii) When norbaeocystin entered, Arg281 rotated to a new conformation to anchor the phosphate group of norbaeocystin; the terminal amine group of norbaeocystin pointed toward the methyl group of SAM, and the methylation reaction occurred; (iv) With the first catalytic step finished, baeocystin would slightly shift along the indole ring and away from the cofactor. Then, the methyl group of baeocystin rotates in the other direction, leaving the amine group toward the cofactor; (v) The new cofactor SAM transfers the methyl group to the baeocystin, producing psilocybin, which will further shift along the indole ring to

Fig. 4 | Structure of 4-hydroxytryptamine kinase PsiK. **a** The overall structure of PsiK in complex with ADP and tryptamine. The ADP and tryptamine molecules are colored yellow and pink, respectively, and shown as sticks. The two Mg^{2+} ions are depicted as green spheres. **b** Surface representation of the PsiK enzyme. **c** The four loop regions and the linker responsible for cofactor and substrate binding are colored as follows: red (Loop 1: aa. 31–36), yellow (Loop 2: aa. 60–72), blue (Loop 3: aa. 221–231), pink (Loop 4: aa. 248–253), and gray (linker: aa. 119–125), respectively. **d** The ADP binding site. The ADP molecule is shown as a stick and colored yellow; the residues involved in ADP binding are colored green and shown as sticks. The water molecules and Mg^{2+} ions are depicted as red and green spheres. The |Fo|-|Fc| map is contoured at 3.0 σ (colored blue). **e** The Mg^{2+} chelating site. The |Fo|-|Fc| map is contoured at 3.0 σ (colored blue). **f** The substrate recognition site of PsiK. The contours of tryptamine and the residues involved in substrate binding are colored purple and green. The |Fo|-|Fc| map is contoured at 3.0 σ (colored blue and purple). **g** The substrate-binding pocket is indicated by a yellow dashed circle. **h** The reaction center of the PsiK enzyme. The catalytic active residue Asp22 is indicated by a brown circle. **i** Modeling 4-hydroxytryptamine into the substrate-binding pocket. The potential movement of the substrate is indicated by a red arrow. **j** The proposed reaction scheme of the PsiK enzyme.

accommodate the two methyl groups; (vi) Finally, the psilocybin substrate will be released from the catalytic pocket with the rotation of Arg281 to the free state without substrate binding.

In vivo activity of the biosynthetic intermediates of psilocybin

Previous studies have reported that psilocybin produces antidepressant effects in mice[45,46]. However, the methylation step produces two unfinished catalytic intermediates structurally quite similar to psilocybin; it is still unclear whether these intermediates have similar biological effects. Therefore, we adopted a 6-day sub-chronic variable stress (SCVS) paradigm in female mice to induce depressive-like behaviors, followed by a single intraperitoneal injection of saline, psilocybin, norbaeocystin, and baeocystin (1 mg/kg) one day after the completion of SCVS, to evaluate the biological effects of these intermediates. The behavioral tests, including the sucrose splash test (ST), social interaction test (SIT), novelty-suppressed feeding (NSF), forced swim test (FST), sucrose preference test (SPT), and the open-field test (OFT), were performed to examine the motivated behaviors and anxiety levels of the mice (Fig. 6a). The behavioral results showed that the SCVS successfully induced weight loss and depression-like behaviors in the female mice (Supplementary Fig. 20a–i).

Compared to the vehicle-injected SCVS mice, the psilocybin- and norbaeocystin-injected SCVS mice showed a significant decrease in their immobility time in the forced swim test and an increased in social interaction time (Fig. 6b, c), indicating that both psilocybin and norbaeocystin alleviated stress-induced depression-like phenotypes and increased motivated behaviors. Notably, the SCVS mice treated with norbaeocystin also showed a reduced latency to eat in the novelty-suppressed feeding test and increased intake of sucrose water in the sucrose preference test, suggesting the anti-anhedonic effects of norbaeocystin (Fig. 6d, e). Meanwhile, no differences were observed among all groups of SCVS mice regarding grooming time in the splash test (Fig. 6f). In the open-field test that measured the anxiety level of the animals, the time spent and distance traveled in the central area of the open field remained unaltered in the SCVS mice treated with psilocybin and its two biosynthesis intermediates (Fig. 6g).

Changes in neuronal activity of the medial prefrontal cortex (mPFC) have been reported in stress-induced depression-like behaviors in mice[47,48]. Our results showed that, compared with the vehicle-injected SCVS mice, norbaeocystin-injected SCVS mice exhibited a significant elevation in c-FOS expression, an indicator of neuronal activity, in the infralimbic PFC (IL-PFC) of SCVS mice (Fig. 6h–l). These findings in SCVS female mice suggest the therapeutic potential of the biosynthetic intermediates of psilocybin, specifically norbaeocystin, in alleviating clinical symptoms of depression.

Discussion

Psilocybin is one of the most attractive psychedelic drugs for coping with mental disorders because it has been shown to require a low dose, be non-addictive, and have high safety[1,2]. Following the elucidation of the biosynthetic pathway for the production of psilocybin in *P. cubensis*[24], bioengineering has led to the production of psilocybin in fungi and bacteria[27–29]. Solving the structures of the enzymes involved in producing psilocybin is essential for selecting highly efficient enzymes to enhance psilocybin production. Here, we have determined the multiple crystal structures of PsiD, PsiK, and PsiM in their apo and substrate-bound forms.

Our structural studies revealed that L-tryptophan decarboxylase PsiD is similar to the PSD superfamily enzyme, featuring self-cleavage activity that produces a β-chain and an α-chain[30,34]. This self-cleavage mechanism is typically found in the pyruvoyl-containing enzymes, which can be mainly divided into two classes: the first is represented by decarboxylases involved in metabolizing amino acids, such as histidine, S-adenosylmethionine, aspartate, and phosphatidylserine, and the second class is represented by reductases[37]. The decarboxylases use a serine residue to induce the serinolysis reaction to achieve the self-cleavage of the proprotein[37]. In contrast, the reductases possess a cysteine instead of the serine residue for the catalytic reaction[49]. However, some decarboxylases and reductases are shown to require an additional factor to facilitate the maturation process of the proprotein, such as the histidine decarboxylase and the L-aspartate-α-decarboxylase[50,51], as well as one of the components of the proline reductase (Prd) complex[49]. Consistent with the typical self-cleavage mechanism, our structure of PsiD unveiled a putative non-classical catalytic triad Glu242-His296-Ser403, as indicated by previous studies that differ from those of *Ec*PSD[30,52,53]. The mutations of the critical residues His296 and Ser403 have resulted in a loss of their decarboxylation abilities. Unfortunately, the mutation of Glu242 to alanine or glutamine is insoluble in our studies, so we could not directly test its impact on the self-cleavage of the PsiD protein. Further studies are needed to evaluate its role in PsiD for self-cleavage and catalytic reactions. Additionally, some PsiD mutants present increased catalytic activity for the L-tryptophan substrate. These observations might be attributed to the enzyme's capacity to accommodate the substrate, thereby promoting the turnover of the reaction.

Only a minor portion of the PsiD protein presented the homodimer conformation in solution, while the main form of the PsiD protein exists as a monomer (Supplementary Fig. 3d). However, the crystal structure of the PsiD (50–439)-Trp complex, which has different cell parameters and contains only two PsiD molecules in the asymmetric unit, presents itself as a homodimer. Additionally, the PISA analysis indicated that the structures of apo-PsiD and PsiD-Trp consist of three identical metastable dimers in their asymmetric unit, while the structure of PsiD (50–439)-Trp contains one homodimer[54]. However, we cannot rule out the possibility that protein concentration in crystallization experiments influences the PsiD enzyme to favor the homodimer conformation; the monomeric state in solution may reflect the true state of PsiD. Further studies are needed to determine the exact status of PsiD and whether the monomeric or dimeric conformation impacts its catalytic activity. The PsiD protein was also indicated to process other substrates directly, such as 4-hydroxy-L-tryptophan and 4-hydroxy-6-methyl-L-tryptophan[26,30]. Our structural studies suggested enough space in the catalytic pocket to accommodate the two substrates without significant clashes (Supplementary Fig. 21a, b). It is also worth noting that although the gene cluster responsible for psilocybin biosynthesis has been identified, research has proposed an

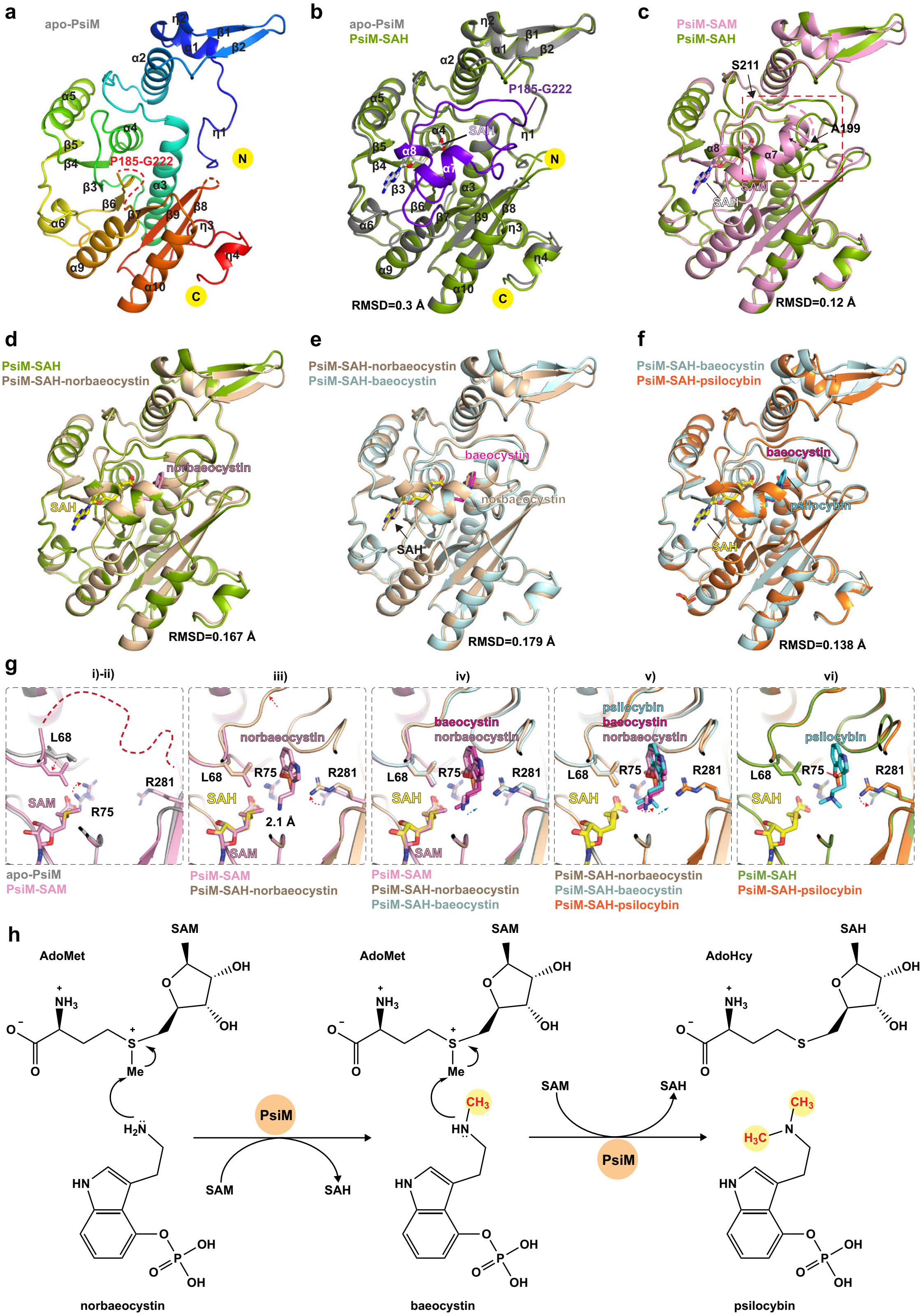

alternative pathway for the decarboxylation step involving a non-canonical aromatic L-amino acid decarboxylase (*Pcnc*AAAD) sourced from *P. cubensis*[55]. The biochemical characterization and crystal structure studies of this enzyme reveal its activity toward L-phenylalanine, L-tyrosine, L-tryptophan, and chloro-tryptophan derivatives. Therefore, this enzyme represents a valuable alternative tool for the metabolic engineering of psilocybin production.

Our structure of the PsiK-ADP-Mg^{2+}-tryptamine complex unveiled the cofactor binding site, the divalent chelation status, and the inactive substrate-binding state by using tryptamine instead of 4-hydroxytryptamine as the substrate. The PsiK showed high structural conservation to the MTR kinases in *Arabidopsis thaliana* and *Bacillus subtilis*. Based on their similarities, we proposed a potential catalytic mechanism for the PsiK enzyme in converting 4-hydroxytryptamine to

Fig. 5 | The methylation processes of psilocybin production. a The overall structure of the apo-PsiM protein is colored in rainbow hues. The missing region in apo-PsiM is indicated by red dashed lines. **b** Structural superposition of apo-PsiM and the PsiM-SAH complex. The structures of apo-PsiM and the PsiM-SAH complex are colored gray and green, respectively. The missing region in the structure of apo-PsiM is colored purple-blue in the PsiM-SAH complex. **c** Structural superposition of PsiM-SAM with PsiM-SAH. The red dashed box indicates the conformationally changed region attributed to the binding of different cofactors. **d** Structural superposition of the PsiM-SAH complex with the PsiM-SAH-norbaeocystin complex. The norbaeocystin and SAH are colored pink and yellow. **e** Structural superposition of the PsiM-SAH-baeocystin complex with the PsiM-SAH-norbaeocystin complex. The baeocystin substrate and SAH cofactor in the PsiM-SAH-baeocystin complex are colored purple and yellow. **f** Structural comparison between the PsiM-SAH-baeocystin complex and the PsiM-SAH-psilocybin complex: the former is colored cyan, while the latter is colored orange. **g** The conformational changes of the residues involved in cofactor and substrate binding. **h** The continuous catalytic scheme of methylation reactions by the PsiM protein.

norbaeocystin. However, due to the control of 4-hydroxytryptamine in China, we could not obtain the natural substrate for the PsiK complex. Future studies are needed to uncover the catalytic mechanism of PsiK in converting 4-hydroxytryptamine into norbaeocystin. Our results also illustrate the stepwise catalytic mechanism of PsiM in adding two methyl groups to the norbaeocystin substrate and validate that the phosphate group is indispensable for the methylation reaction. When we prepared the manuscript, a similar structural study of PsiM was published[44]. In line with that study, our studies also suggest that the PsiM protein is a homolog of human METTL16[44]. Additionally, our studies confirmed that human METTL16 could not catalyze norbaeocystin or baeocystin to psilocybin, as validated by our TLC experiments, suggesting that human METTL16 plays no role in the metabolic turnover of psilocybin or its derivate psilocin. These analyses could increase the safety profile of the future use of psilocybin-related drugs. Other detailed analyses between the PsiM and METTL16 protein can be found in Supplementary Note 3 and the recently published work[44].

In mushrooms, other tryptamine derivatives such as psilocin, baeocystin, norbaeocystin, aeruginascin, and norpsilocin may also influence the efficacy of psilocybin treatment[10,56]. Hence, we evaluated the therapeutic effects of the precursors of psilocybin through the SCVS model of depression in female mice. It is worth noting that therapeutic doses of psilocybin have been reported to produce adverse effects, such as anxiety, paranoia, and prolonged visual perceptual effects[57,58]. In our SCVS model of depression, we showed the therapeutic effect of the biosynthetic intermediate norbaeocystin to be comparable to psilocybin in alleviating depression-like behaviors and anhedonia in SCVS female mice without the anxiogenic effect. Our animal studies align closely with a recent investigation into the pharmacological and behavioral impacts of tryptamine derivatives, in which the researchers showed that, unlike psilocybin, neither baeocystin nor norbaeocystin elicited significant head twitch responses (HTR)[59]. While they observed immediate antidepressant-like effects of psilocybin and norbaeocystin in non-stressed rats[59], our study demonstrated sustained effects (spanning 4 days) in female mice subjected to the SCVS paradigm. Notably, prior studies have reported persistent antidepressant-like effects of psilocybin injected at low doses (1 mg/kg) administered to rodent models of depression[46,60]. These earlier findings are not only in line with our behavioral studies on psilocybin but also underscore the reliability of the antidepressant-like effects of norbaeocystin.

However, although these results support our findings, there are inconsistent studies regarding the antidepressant-like effects of psilocybin. These effects may be attributed to various factors, such as differences in administration doses and frequency[45,46,61,62], stress paradigms[45,46], timing of assessment[45,63], and genetic background of animals[64,65]. For example, earlier studies have highlighted inconsistent behavioral outcomes of psilocybin in the FST experiments, which can be attributed to variations in assessment timing and the genetic backgrounds of the animals[45,60,64,65]. Nevertheless, most studies on psilocybin or psilocin showed a significant influence on the FST experiments at similar doses (1–1.5 mg/kg)[46,59–61], supporting our findings that female mice receiving SCVS exhibited reduced immobility time. Similar to the FST experiments, different outcomes can be observed in the SPT experiments. The increased sucrose intake in our psilocybin-treated SCVS female mice showed no significant differences, possibly due to varying stress levels[45] or the doses of psilocybin administered[62]. In the NSF experiments, stress levels and administration doses also influenced the efficacy of psilocybin[46,66]. In our study, a single dose of psilocybin (1 mg/kg) has no effect on reducing food intake latency in SCVS female mice, whereas a higher dose of psilocybin (5 mg/kg) was indicated to reduce the latency to feed significantly[66]. In the SIT experiments, a single dose of psilocin (1.5 mg/kg) administered to unstressed adult male mice did not produce any further increase in social interaction time during a three-chamber social test 24 h post-injection[61]. However, our study showed that a single dose of psilocybin (1 mg/kg) increased social interaction among SCVS females 24 h after injection. The varying genetic backgrounds may influence the efficacy of psilocybin in social interaction performance[64]. In the OFT experiments, consistent with prior observations in adult male mice[58], our studies revealed that a 1 mg/kg psilocybin treatment did not affect anxiety levels. However, higher doses of psilocybin (3 mg/kg, 5 mg/kg) were shown to produce varying effects on anxiety-like behaviors[58]. Finally, despite administering the same dose of psilocybin as in the previous studies[45,63], no acute HTR was observed in our experiment. This may be because the HTR typically peaked within 15 min after psilocybin administration and then gradually declined and ceased within 2 h, whereas the behavioral outcomes were assessed one day following the drug injection in our study. More detailed illustrations of the variations in the behavioral experiments can be found in Supplementary Note 4. Overall, before referring to the results of antidepressants in animals, one should carefully examine the differences in experimental conditions.

In conclusion, our studies provide a practical view and structural basis for further bioengineering production of psilocybin and its derivatives through synthetic biology methods.

Methods

Animals

Three- to four-month-old female wildtype C57BL/6J mice, with a body weight of (20 ± 5) g, were obtained from the Zhuhai Bai Shi Tong Animal Center (Zhuhai, China). The animals were kept in a specific pathogen-free environment, with 4–5 animals per cage. The temperature (23 ± 2 °C) and humidity (50–60%) were kept stable. The animals had free access to food and water. Animals were subjected to a 12 h/12 h dark/light cycle daily. All animal studies were reviewed and approved by the Institutional Animal Care and Use Committee of Sun Yat-Sen University (approval number: SYSU-IACUC-2023-000057).

Protein expression and purification

Plasmid encoding full-length *Psilocybe cubensis (Psychedelic mushroom)* PsiD (Uniprot ID: P0DPA6) was ordered from Tsingke Biotechnology Co., Ltd. In brief, the full-length or truncated *psiD* gene was ligated into a modified pET-28a plasmid between *BamH*I and *Xho*I, and the pET-28a plasmid carries N-terminal His_6-SUMO fusions and an Ulp1 cleavage site upstream of *BamH*I. Mutations were generated based on overlap PCR. All the constructs were confirmed by DNA sequencing. The wildtype PsiD and its mutants were transformed into *Escherichia coli* BL21 (DE3) strain to produce target proteins. *E. coli* cells were cultured in LB medium at 37 °C with 50 mg/mL kanamycin until the OD_{600} reached 0.6–0.8.

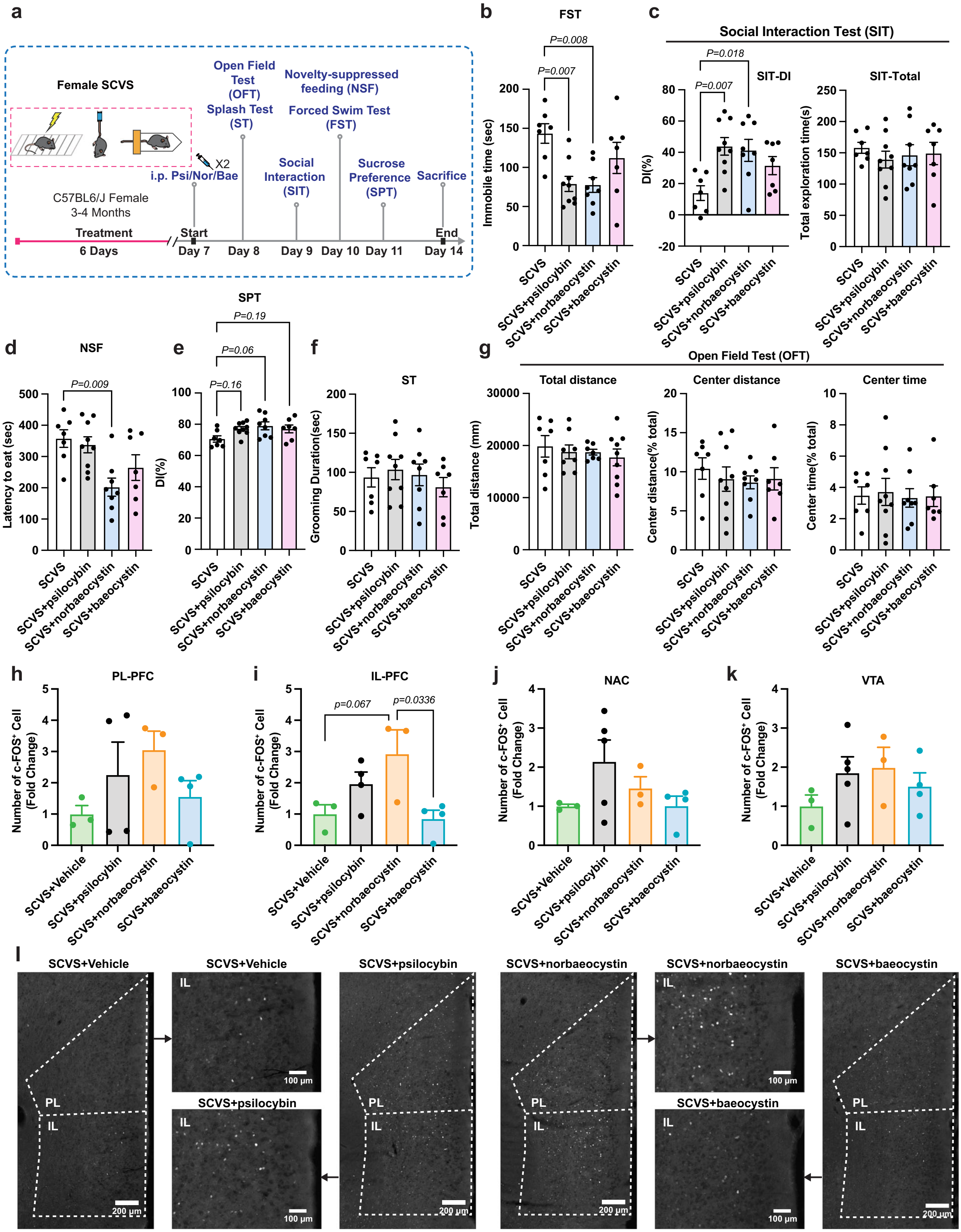

The bacteria were induced with 0.2 mM isopropyl-β-d-thiogalactoside (IPTG) at 18 °C for 14–20 h. Bacteria were collected by centrifugation, resuspended in buffer containing 20 mM Tris-HCl pH 8.0, 500 mM NaCl, 25 mM imidazole pH 8.0, and then lysed by high pressure. Cell extracts were centrifuged at 37,157 g for 1 h at 4 °C. Supernatants were purified with Ni-NTA (GE), the target protein was washed with lysis buffer and then eluted with elution buffer containing 20 mM Tris-HCl pH 8.0, 500 mM NaCl and 500 mM imidazole. Ulp1 protease was added to remove the N-terminal His_6-SUMO fusions of the recombinant protein and dialyzed with lysis buffer for 3 h. Then, the mixture was applied to another Ni-NTA resin to remove the protease and uncleaved proteins. Eluted proteins were concentrated by centrifugal ultrafiltration, loaded onto a pre-equilibrated HiLoad 16/600 Superdex 200-pg column, and eluted at a 1 mL/min flow rate with the same buffer containing 10 mM

Fig. 6 | Antidepressant effects of psilocybin and its biosynthetic intermediates. **a** The experimental timeline of the sub-chronic variable stress (SCVS) paradigm, behavioral tests, and tissue collection (sacrifice) for the four groups of female mice. **b** Immobility time of mice in the forced swim test (FST). **c** Differential index (DI) and total exploration time in the social interaction test (SIT). **d** Time of the latency to eat in the novelty-suppressed feeding test (NSF). **e** Quantification of sucrose water intake in the sucrose preference test (SPT). **f** Grooming duration in the splash test (ST). **g** Quantification of the total distance traveled, the distance traveled in the center zone as a percentage of the total distance traveled, and the time spent in the center zone as a percentage of the total time in the open-field test (OFT). Quantitative analyses of the density of c-FOS-positive cells in (**h**) PL-PFC, (**i**) IL-PFC, (**j**) NAc, and (**k**) VTA brain regions among the four groups of female mice. PL-PFC, prelimbic prefrontal cortex; IL-PFC, infralimbic prefrontal cortex; NAc, nucleus accumbens; VTA, ventral tegmental area. **l** Representative images of c-FOS staining in the IL-PFC brain region (scale bar: PL+IL: 200 µm, IL only: 100 µm). SCVS + Vehicle: SCVS mice that received saline injection; SCVS + psilocybin: SCVS mice that received psilocybin injection; SCVS + norbaeocystin: SCVS mice that received norbaeocystin injection; SCVS + baeocystin: SCVS mice that received baeocystin injection. **b**–**g** $N = 7, 9, 8, 7$ mice per group, **h**, **i** $N = 3, 4, 3, 4$ mice per group, **j**, **k** $N = 3, 5, 3, 4$ mice per group. All data are presented as mean ± SEM and analyzed using one-way ANOVA followed by Tukey's post hoc test.

Tris-HCl pH 8.0, and 100 mM NaCl. Purified fractions were pooled together and concentrated by centrifugal ultrafiltration. The concentration was determined by A_{280} for further crystallization trials and biochemical characterization of the enzyme activities. A plasmid encoding *Psilocybe cubensis* (*Psychedelic mushroom*) PsiM (Uniprot ID: P0DPA9) was ordered from Tsingke Biotechnology Co., Ltd. All the purification procedures were the same as those for PsiD. The concentration was determined by A_{280} for further crystallization trials and biochemical characterization of the enzyme activities. For the PsiK production, the plasmid encoding *Psilocybe cubensis (Psychedelic mushroom)* PsiK (Uniprot ID: P0DPA8) was also ordered from Tsingke Biotechnology Co., Ltd. All the purification procedures were the same as those for PsiD; however, the final gel filtration buffer was changed to 10 mM Tris pH 8.0, 100 mM NaCl for further crystallization trials and biochemical experiments. The human *METTL16* gene was PCR amplified from the human cDNA and subcloned into the modified pET-28a-Sumo plasmid to express the truncated METTL16 (1–310) protein. All the purification procedures were the same as those for PsiD, but the final gel filtration buffer was changed to 10 mM Tris pH 8.0, 100 mM NaCl, and 1 mM DTT for further biochemical experiments.

Crystallization and data collection

All the crystals were crystallized using the sitting drop vapor diffusion method by mixing 0.2 µL of protein and 0.2 µL of reservoir solution at 18 °C. The crystals picked for data collection were all soaked in cryoprotectants containing the crystallization conditions, supplemented with 20% glycerol, and were fast-frozen in liquid nitrogen. Diffraction data were collected from the National Facility for Protein Science in Shanghai (NFPS) at the Shanghai Synchrotron Radiation Facility (SSRF). The crystallization conditions are listed below:

1) The crystal of apo-PsiD suitable for X-ray diffraction was grown in a reservoir solution consisting of 0.2 M Ammonium acetate, 0.1 M Sodium citrate pH 5.6, 30% w/v Polyethylene glycol 4000.
2) The crystals of the PsiD-Trp complex suitable for X-ray diffraction were grown in a reservoir solution consisting of 0.2 M Sodium chloride, 0.1 M Tris pH 8.5, 25% w/v Polyethylene glycol 3350.
3) The crystals of the PsiD (50–439)-Trp complex suitable for X-ray diffraction were grown in a reservoir solution consisting of 0.1 M Magnesium formate dihydrate, 15% w/v Polyethylene glycol 3350.
4) The crystals of PsiK-ADP-Mg^{2+}-Tryptamine complex suitable for X-ray diffraction were grown in a reservoir solution consisting of 20% (w/v) PEG 8000, 0.1 M Tris base/Hydrochloric acid pH 8.5, 0.1 M Magnesium chloride, and 20% (v/v) PEG 400.
5) The crystals of apo-PsiM suitable for X-ray diffraction were grown in a reservoir solution consisting of 0.2 M Magnesium chloride, 0.1 M Tris pH 8.5, 30% w/v PEG 4000.
6) The crystals of PsiM-SAM suitable for X-ray diffraction were grown in a reservoir solution consisting of 0.2 M Ammonium acetate, 0.1 M Sodium acetate trihydrate pH 4.6, 30% w/v Polyethylene glycol 4000.
7) The crystals of the PsiM-SAH complex suitable for X-ray diffraction were grown in a reservoir solution consisting of 1.2 M Potassium phosphate (dibasic)/0.8 M Sodium phosphate (monobasic), 0.1 M Sodium acetate/Acetic acid pH 4.5.
8) The crystals of PsiM-SAH-norbaeocystin suitable for X-ray diffraction were grown in a reservoir solution consisting of 40% (v/v) Isopropanol, 0.1 M Imidazole/Hydrochloric acid pH 6.5, 15% (w/v) PEG 8000.
9) The crystals of PsiM-SAH-baeocystin suitable for X-ray diffraction were grown in a reservoir solution consisting of 0.1 M HEPES pH 7.5, 20% w/v Polyethylene glycol 10,000.
10) The crystals of PsiM-SAH-psilocybin suitable for X-ray diffraction were grown in a reservoir solution consisting of 0.2 M Sodium acetate, 0.1 M Sodium cacodylate pH 6.5, 30% w/v PEG 8000.

Structure determination and refinement

For the apo-PsiD structure, the diffraction dataset was processed and scaled using XDS[67]. The phase was determined by molecular replacement using the program Phaser with the predicted structure (Uniprot ID: P0DPA6) by AlphaFold2 as the search model[31]. Cycles of refinement and model building were carried out using PHENIX and COOT, respectively[68,69]. For the PsiD-Trp and PsiD (50–439)-Trp structures, the diffraction datasets were also processed and scaled using XDS[67]. The phase was determined by molecular replacement using the program Phaser with the structure of apo-PsiD as the search model[70]. Cycles of refinement and model building were carried out using PHENIX and COOT[68,69]. For the PsiK-ADP-Mg^{2+}-Tryptamine structure, the phase was determined by molecular replacement using the program Phaser with the predicted structure (Uniprot ID: P0DPA8) by AlphaFold2 as the search model. Cycles of refinement and model building were carried out using PHENIX and COOT, respectively[68,71]. For the apo-PsiM structure, the diffraction dataset was processed and scaled using XDS[67]. The phase was determined by molecular replacement using the program Phaser with the predicted structure (Uniprot ID: P0DPA9) by AlphaFold2 as the search model. Cycles of refinement and model building were carried out using PHENIX and COOT, respectively[68,71]. For the other structures, including PsiM-SAM, PsiM-SAH, PsiM-SAH-norbaeocystin, PsiM-SAH-baeocystin, and PsiM-SAH-psilocybin, the diffraction datasets were also processed and scaled using XDS[67]. The phase was determined by molecular replacement using the program Phaser with the structure of apo-PsiM as the search model[70]. Cycles of refinement and model building were carried out using PHENIX and COOT, respectively[68,71]. The details of data collection and processing are presented in Supplementary Table 1. All structure figures were prepared with PyMOL.

Decarboxylation assay

The enzymatic assays were performed in a buffer containing 10 mM Tris-HCl pH 8.0 and 100 mM NaCl. For the decarboxylation reactions of the wildtype PsiD, 20 mM substrate L-tryptophan and gradient-increased PsiD concentrations ranging from 20 to 100 µM were individually included in the total volume of 20 µL reaction systems. The reaction systems were incubated at 37 °C for 1 h. To test the PsiD mutants' activities, 100 µM purified wildtype PsiD protein or its mutant proteins and 20 mM substrate L-tryptophan were individually included in the total volume of 20 μL reaction systems. All the reactions were incubated for 1 h at 37 °C. For testing the impact of the pH value on the activity of wildtype PsiD, 100 μM purified wildtype PsiD protein and 20 mM substrate L-tryptophan were individually included in a total volume of 20 μL reaction systems. The assays were performed in a buffer containing 100 mM NaCl and 10 mM Tris-HCl, with the pH ranging from 7.4 to 9.0. The reaction systems were incubated at 37 °C for 1 h. To determine the enzyme activities of the wildtype PsiD, PsiD (30–439), PsiD (50–439), PsiD (1–439) S403A, and PsiD (1–439) W27A, 100 μM purified proteins of these constructs and 20 mM substrate L-tryptophan were each included in a 20 μL reaction system. The enzymatic assays were performed in the buffer containing 10 mM Tris-HCl pH 8.0 and 100 mM NaCl. The reaction systems were incubated at 37 °C for 30 s to 14 min or 1 h.

All the samples were spotted as follows: 1 μL aliquots were taken and spotted on a pre-saturated (1 h) aluminum plate coated with silica gel 60 F254 and developed for 3 h. The spots were 2 cm from the bottom of the plate, and the plates were developed with N-butyl alcohol: H_2O: Ethanoic acid (12:5:3) as solvents. The spots were exposed to UV light at 254 nm for visualization. All data points were obtained in three replicate experiments. Data are expressed as the mean ± SEM unless otherwise noted.

In vitro methylation assay

The enzymatic assays were performed in a buffer containing phosphate buffer (50 mM NaH_2PO_4 pH 7.4). For testing the activities of the wildtype or mutant PsiM proteins or the METTL16 (1–310), 200 μM of purified wildtype PsiM protein or its mutant proteins and 2.5 mM substrate norbaeocystin or baeocystin, and 2.5 mM cofactor SAM were included in a total volume of 20 μL reaction system. All the reactions were incubated for 1 h at 25 °C. Aliquots of 1 μL were taken and spotted on a pre-saturated (1 h) aluminum plate coated with silica gel 60 F254 and developed for 3 h. The spots were 2 cm from the bottom of the plate and 1.4 cm apart, and the plates were developed with N-butyl alcohol: H_2O: Ethanoic acid (12:5:3) as the solvents. The spots were exposed to UV light at 254 nm for visualization. All data points were obtained from three replicate experiments. Data are expressed as the mean ± SEM unless otherwise noted.

Analytical gel filtration

PsiD mutant proteins were purified using the same procedure as wildtype PsiD. Analytical gel filtration chromatography was performed at 4 °C using a Superdex 200 10/300 global column (Cytiva) pre-equilibrated in 10 mM Tris pH 8.0 and 100 mM NaCl. All samples, including the wildtype PsiD, S403A, and R135A/Q136A, were injected at a flow rate of 0.3 mL/min, respectively.

Liquid chromatography and mass spectrometry

The enzymatic reaction products were detected by the Ultimate 3000 (HPLC)-Q Exactive plus mass spectrometer (MS) in positive mode. The linear separation process was performed at 25 °C with a gradient of acetonitrile (ACN) from 5% to 100% within 7 min at a flow rate of 0.3 mL/min. Solvent A was 0.1 % aqueous formic acid (FA), and solvent B was ACN + 0.1% FA. High-resolution mass spectra were recorded on the Thermo Q-Exactive Orbitrap MS, fitted with an ACQUITY UPLC BEH C18 column (130 A, 1.7 μm, 100 × 2.1 mm). All MS spectra were obtained in data-dependent mode with one MS full-scan ranging from 70 to 1050 Dalton. The parent ions for reactants and products were 205.10 and 161.11, respectively.

To validate the pyruvoyl prosthetic group instead of the serine residue that exists in the N-terminal of the α-chain within the mature PsiD enzyme, the peptides of the α-chain were extracted from the SDS-PAGE using an 80% ACN aqueous solution. The obtained peptide solution was freeze-dried. 1 μg of trypsin (dissolved in 100 μL of 10 mM NH4CO3) was added, followed by digestion at 37 °C overnight. The tryptic digests were analyzed by a Fusion MS in positive mode. The gradient is from 6% to 35% ACN in 30 min. All MS and MS/MS spectra were obtained in data-dependent mode with one MS full-scan ranging from 300 to 1800, followed by 10 MS/MS scans. The raw files obtained were uploaded to Proteome Discoverer (PD, version 2.1) and searched against the self-written database (sequence: SFALGLRKDCRAEIVEKFTEPGTVIRINEVVAALKA) to show the modifications of identified peptides. The parameters for searching were set as follows: enzyme, trypsin; missed cleavages, two; variable modifications, C3H2O2 (S, 70 Da). The peptide tolerance and MS/MS tolerance were 10 ppm and 0.02 Da, respectively. The ascertained false discovery rate (FDR) for all the identified peptides was less than 1%.

Sub-chronic variable stress (SCVS)

Animals were adapted to the environment for 3–4 days before the experiments. The mice were then handled for 3 days before being subjected to different stressors every day for 6 days. On the first and fourth days, the mice (5–10 grouped in the shock chamber, Med Associates, Vermont, USA) received one hundred foot-shocks (0.45 mA, 1 s delivered at random intervals for 1 h); on the second and fifth days, they were subjected to tail suspension stress; on the third and sixth days, the mice were restrained in the conical tube for 1 h.

Drug injection

Psilocybin, norbaeocystin, and baeocystin powders were dissolved in a 0.9% sterile saline solution, and the mice were intraperitoneally injected (1 mg/kg) on the morning of the next day after the completion of SCVS. For the vehicle control group, the mice were injected with 0.9% sterile saline solution. Behavioral testing was conducted on the days following the injection.

Behavioral tests

Depressive-like and anxiety-like behaviors were assessed within one week after the completion of SCVS. On the test day, mice were placed in the testing room for habituation for 1–2 h. The behavioral testing apparatus was cleaned with 75% ethanol between animals. The order of the behavioral tests was specified in the experimental timeline of the figures.

Splash test (ST)

The test was conducted in a standard mouse cage under red light (60–80 Lux) in a sound-insulated chamber. The mice were allowed to move freely for 1 min to habituate to the arena. Then, the dorsal coat of the mice was sprayed 3 times with a 10% sucrose solution and videotaped for 5 min. The time spent grooming was recorded using a stopwatch by a researcher blinded to the experimental groups.

Social interaction test (SIT)

An unfamiliar female mouse (social mouse) was used for the social interaction test and acclimated in a round plastic cage for 10 min each day for 3 days prior to the beginning of the test to reduce the anxiety level. Social interaction was measured in a 60 × 40 × 20 cm box, divided into three chambers by two transparent dividing walls, under red light (60–80 Lux) in a sound-insulated chamber. On the test day, the test mouse was first allowed to explore the box with two empty enclosures for 10 min. Then, the social mouse was placed in one of the enclosures, while a toy mouse was placed in the other enclosure. The test mouse was placed back in the box for 10 min and allowed for free exploration. Both phases of the test were videotaped and analyzed by a researcher blinded to the experimental groups. The interaction time between the test mouse and the social mouse was recorded as A, and the interaction time between the test mouse and the toy mouse was recorded as B. The index of social interaction was calculated as (A−B)/(A + B) × 100%.

Novelty-suppressed feeding (NSF) test

Mice were weighed, and all food was removed from their cages 24 h prior to the test. During the test, the mouse was placed in an empty white plastic box (30 × 30 × 30 cm) without bedding. A small piece of a mouse pellet was placed in the center of the arena, and the mouse was placed in the corner. The box was enclosed in a sound-insulated chamber, illuminated under red light (60–80 Lux). The latency to begin food consumption in a 10-min test was measured by a researcher blinded to the experimental groups.

Open-field test (OFT)

The open-field arena was a white box (40 × 40 × 40 cm) illuminated with red light (60–80 Lux), placed inside a sound-insulated chamber. After wiping the box with 75% alcohol, the mouse was placed into the corner of the box and allowed to move freely. The total distance traveled, as well as the distance traveled and time spent in the center zone (20 × 20 cm), were tracked and analyzed by the DigBehv software (version 4.1.7.171129, Ji-Liang, Shanghai, China).

Forced swim test (FST)

Mice were placed into a 5 L glass beaker containing 3.5 L of water at 24–25 °C under white light (210–280 Lux). The mice were subjected to the FST for 6 min, and their activity was video-recorded. Each video was analyzed by a researcher blinded to the experimental groups and scored for immobility time over the last 4 min duration, which was defined as the absence of any body movement except that necessary for the mice to keep their heads above the water.

Sucrose preference test (SPT)

Each mouse was individually housed in a cage with two drinking bottles. All mice had access to chow diet ad libitum. On day 1, two bottles of 1% sucrose solution were placed at the same time. The mice adapted to the environment and were allowed to drink freely for 24 h. On day 2, the weight of a bottle of drinking water (M1 water) and the weight of a bottle of 1% sucrose solution (M1 sugar) were recorded and placed in the mouse cage. The mice were allowed to drink freely for 24 h, and the remaining weight of drinking water (M2 water) and sucrose solution (M2 sugar) was recorded. On day 3, the positions of the two drinking bottles were swapped to eliminate the bias caused by position preference. The weight of a new bottle of drinking water (M3 water) and a new bottle of 1% sucrose solution (M3 sugar) were recorded. 24 h later, the weight of the remaining drinking water (M4 water) and sucrose solution (M4 sugar) was recorded. Sucrose preference was calculated as follows: [(M1 sugar−M2 sugar) + (M3 sugar−M4 sugar)]/[(M1 water −M2 water) + (M1 sugar−M2 sugar) + (M3 water−M4 water) + (M3 sugar −M4 sugar)] × 100%

Immunofluorescence staining and image analysis

Mice were anesthetized with intraperitoneal (i.p.) injection of sodium pentobarbital (100 mg/kg body weight), transcardially perfused with PBS for 2 min, followed by 4% paraformaldehyde in PBS for 5 min at a rate of 10 mL/min. The brains were then harvested and postfixed in 4% paraformaldehyde in PBS overnight at 4 °C, followed by cryoprotection in 30% sucrose in PBS for 2–3 days at 4 °C. 30–40 μm coronal brain sections were collected using a cryostat. One coronal section containing the mPFC (at ~1.77 and 1.97 mm anterior to the Bregma), one section containing the NAc (at ~0.73 and 1.21 mm anterior to the Bregma), and one section containing the VTA (at ~2.91 and 3.15 mm posterior to the Bregma) were sampled for free-floating immunofluorescence staining. The brain regions of interest were determined based on the 4th edition of "The Mouse Brain in Stereotaxic Coordinates" by Paxinos and Franklin. The sections were blocked with a solution containing 5% goat serum, 1% bovine serum albumin, and 0.4% Triton X-100 in PBS for 2 h at room temperature. Subsequently, they were incubated with the primary antibody of c-FOS (Cell Signaling Technology, cat#: 2250, 1:750) in the blocking buffer for ~24 h at 4 °C, followed by 10 min rinse of PBS with 0.4% Triton X-100 for three times, and incubated with the secondary antibody (Goat anti-rabbit IgG(H+L) Alexa Fluor 488, Thermo Fisher, A11034,1:800) in the blocking buffer for 2 h at room temperature. The sections were then washed three times and mounted onto glass slides. Images were acquired using an epi-fluorescent microscope (Eclipse Ni-U, Nikon, Japan) and analyzed with ImageJ (version 1.52n, NIH, USA).

Statistical analysis

Statistical analysis was performed with Prism v10.0 (GraphPad Software, Boston, MA). All data are presented as the mean ± SEM. For multiple-group comparison, one-way ANOVA with Tukey's post hoc test was used. $p < 0.05$ was considered statistically significant.

Reporting summary

Further information on research design is available in the Nature Portfolio Reporting Summary linked to this article.

Data availability

The coordinates generated in this study have been deposited in the Protein Data Bank under accession codes 8X4Q (apo-PsiD), 8X4S (PsiD-Trp), 8ZIA (PsiD (50–439)-Trp), 8ZIC (PsiK-ADP-Mg^{2+}-Trp), 8ZIE (apo-PsiM), 8ZIG (PsiM-SAM), 8ZIH (PsiM-SAH), 8ZII (PsiM-SAH-norbaeocystin), 8ZIM (PsiM-SAH-baeocystin), and 8ZIO (PsiM-SAH-psilocybin). PDB codes of previously published structures used in this study are 7CNY (*Ec*PSD), 2PYW (*At*MTK), 2PUN (*Bs*MTNK), and 6DU4 (*Hs*METTL16). The mass spectrometry data have been deposited to the ProteomeXchange Consortium via the PRIDE partner repository with the dataset identifier PXD061358[72]. The LC/MS raw data for detecting enzymatic reaction products have been deposited in the BMRbig database (https://bmrbig.org/) under the accession number bmrbig113 [https://bmrbig.org/released/bmrbig113]. Additional information and/or materials related to this study will be made available through a material transfer agreement (MTA) upon request to the corresponding authors. Source data are provided as a Source Data file. Source data are provided with this paper.

References

1. Rehm, J. & Shield, K. D. Global burden of disease and the impact of mental and addictive disorders. *Curr. Psychiatry Rep.* **21**, 10 (2019).
2. Nutt, D., Erritzoe, D. & Carhart-Harris, R. Psychedelic psychiatry's brave new world. *Cell* **181**, 24–28 (2020).
3. Nichols, D. E. Psilocybin: from ancient magic to modern medicine. *J. Antibiot.* **73**, 679–686 (2020).
4. Passie, T., Seifert, J., Schneider, U. & Emrich, H. M. The pharmacology of psilocybin. *Addict. Biol.* **7**, 357–364 (2002).
5. Griffiths, R. R. et al. Psilocybin produces substantial and sustained decreases in depression and anxiety in patients with life-threatening cancer: a randomized double-blind trial. *J. Psychopharmacol.* **30**, 1181–1197 (2016).
6. Carhart-Harris, R. L. et al. Psilocybin with psychological support for treatment-resistant depression: six-month follow-up. *Psychopharmacology* **235**, 399–408 (2018).
7. Bogenschutz, M. P. et al. Psilocybin-assisted treatment for alcohol dependence: a proof-of-concept study. *J. Psychopharmacol.* **29**, 289–299 (2015).
8. Johnson, M. W., Garcia-Romeu, A., Cosimano, M. P. & Griffiths, R. R. Pilot study of the 5-HT2AR agonist psilocybin in the treatment of tobacco addiction. *J. Psychopharmacol.* **28**, 983–992 (2014).
9. Fricke, J., Lenz, C., Wick, J., Blei, F. & Hoffmeister, D. Production options for psilocybin: making of the magic. *Chemistry* **25**, 897–903 (2019).
10. Lowe, H. et al. The therapeutic potential of psilocybin. *Molecules* **26**, https://doi.org/10.3390/molecules26102948 (2021).

11. Hofmann, A. et al. Psilocybin and psilocin, two psychotropic substances in Mexican magic mushrooms. *Helv. Chim. Acta* **42**, 1557–1572 (1959).
12. Hofmann, A., Heim, R., Brack, A. & Kobel, H. [Psilocybin, a psychotropic substance from the Mexican mushroom Psilicybe mexicana Heim]. *Experientia* **14**, 107–109 (1958).
13. Johnson, M. W. & Griffiths, R. R. Potential therapeutic effects of psilocybin. *Neurotherapeutics* **14**, 734–740 (2017).
14. Wieczorek, P. P. et al. Chapter 5 - Bioactive Alkaloids of Hallucinogenic Mushrooms. In: *Studies in Natural Products Chemistry*. Vol. 46 (ed. Rahman Atta ur) (Elsevier, 2015). https://doi.org/10.1016/B978-0-444-63462-7.00005-1.
15. Schultes, R. E. Hallucinogens of plant origin. *Science* **163**, 245–254 (1969).
16. Hasler, F., Bourquin, D., Brenneisen, R., Bar, T. & Vollenweider, F. X. Determination of psilocin and 4-hydroxyindole-3-acetic acid in plasma by HPLC-ECD and pharmacokinetic profiles of oral and intravenous psilocybin in man. *Pharm. Acta Helv.* **72**, 175–184 (1997).
17. Tyls, F., Palenicek, T. & Horacek, J. Psilocybin-summary of knowledge and new perspectives. *Eur. Neuropsychopharmacol.* **24**, 342–356 (2014).
18. Geiger, H. A., Wurst, M. G. & Daniels, R. N. DARK classics in chemical neuroscience: psilocybin. *ACS Chem. Neurosci.* **9**, 2438–2447 (2018).
19. Nichols, D. E. Psychedelics. *Pharmacol. Rev.* **68**, 264–355 (2016).
20. Kargbo, R. B. Psilocybin therapeutic research: the present and future paradigm. *ACS Med. Chem. Lett.* **11**, 399–402 (2020).
21. Mithoefer, M. C., Grob, C. S. & Brewerton, T. D. Novel psychopharmacological therapies for psychiatric disorders: psilocybin and MDMA. *Lancet Psychiatry* **3**, 481–488 (2016).
22. Fricke, J. et al. Scalable hybrid synthetic/biocatalytic route to psilocybin. *Chemistry* **26**, 8281–8285 (2020).
23. Kargbo, R. B. et al. Direct phosphorylation of psilocin enables optimized cGMP kilogram-scale manufacture of psilocybin. *ACS Omega* **5**, 16959–16966 (2020).
24. Fricke, J., Blei, F. & Hoffmeister, D. Enzymatic synthesis of psilocybin. *Angew. Chem. Int. Ed. Engl.* **56**, 12352–12355 (2017).
25. Reynolds, H. T. et al. Horizontal gene cluster transfer increased hallucinogenic mushroom diversity. *Evol. Lett.* **2**, 88–101 (2018).
26. Fricke, J. et al. Enzymatic route toward 6-methylated baeocystin and psilocybin. *ChemBioChem* **20**, 2824–2829 (2019).
27. Hoefgen, S. et al. Facile assembly and fluorescence-based screening method for heterologous expression of biosynthetic pathways in fungi. *Metab. Eng.* **48**, 44–51 (2018).
28. Adams, A. M. et al. In vivo production of psilocybin in E. coli. *Metab. Eng.* **56**, 111–119 (2019).
29. Milne, N. et al. Metabolic engineering of Saccharomyces cerevisiae for the de novo production of psilocybin and related tryptamine derivatives. *Metab. Eng.* **60**, 25–36 (2020).
30. Schafer, T., Kramer, K., Werten, S., Rupp, B. & Hoffmeister, D. Characterization of the gateway decarboxylase for psilocybin biosynthesis. *ChemBioChem* **23**, e202200551 (2022).
31. Jumper, J. et al. Highly accurate protein structure prediction with AlphaFold. *Nature* **596**, 583–589 (2021).
32. Watanabe, Y., Watanabe, Y. & Watanabe, S. Structural basis for phosphatidylethanolamine biosynthesis by bacterial phosphatidylserine decarboxylase. *Structure* **28**, 799–809.e5 (2020).
33. Cho, G., Lee, E. & Kim, J. Structural insights into phosphatidylethanolamine formation in bacterial membrane biogenesis. *Sci. Rep.* **11**, 5785 (2021).
34. Schuiki, I. & Daum, G. Phosphatidylserine decarboxylases, key enzymes of lipid metabolism. *IUBMB Life* **61**, 151–162 (2009).
35. Choi, J. Y., Duraisingh, M. T., Marti, M., Ben Mamoun, C. & Voelker, D. R. From protease to decarboxylase: the molecular metamorphosis of phosphatidylserine decarboxylase. *J. Biol. Chem.* **290**, 10972–10980 (2015).
36. Ogunbona, O. B., Onguka, O., Calzada, E. & Claypool, S. M. Multitiered and cooperative surveillance of mitochondrial phosphatidylserine decarboxylase 1. *Mol. Cell. Biol.* **37**, https://doi.org/10.1128/MCB.00049-17 (2017).
37. van Poelje, P. D. & Snell, E. E. Pyruvoyl-dependent enzymes. *Annu. Rev. Biochem.* **59**, 29–59 (1990).
38. Voelker, D. R. Phosphatidylserine decarboxylase. *Biochim. Biophys. Acta* **1348**, 236–244 (1997).
39. Li, Q. X. & Dowhan, W. Studies on the mechanism of formation of the pyruvate prosthetic group of phosphatidylserine decarboxylase from Escherichia coli. *J. Biol. Chem.* **265**, 4111–4115 (1990).
40. Holm, L. Using Dali for protein structure comparison. *Methods Mol. Biol.* **2112**, 29–42 (2020).
41. Ku, S. Y., Cornell, K. A. & Howell, P. L. Structure of Arabidopsis thaliana 5-methylthioribose kinase reveals a more occluded active site than its bacterial homolog. *BMC Struct. Biol.* **7**, 70 (2007).
42. Ku, S. Y. et al. Structures of 5-methylthioribose kinase reveal substrate specificity and unusual mode of nucleotide binding. *J. Biol. Chem.* **282**, 22195–22206 (2007).
43. Matte, A., Tari, L. W. & Delbaere, L. T. How do kinases transfer phosphoryl groups? *Structure* **6**, 413–419 (1998).
44. Hudspeth, J. et al. Methyl transfer in psilocybin biosynthesis. *Nat. Commun.* **15**, 2709 (2024).
45. Hesselgrave, N., Troppoli, T. A., Wulff, A. B., Cole, A. B. & Thompson, S. M. Harnessing psilocybin: antidepressant-like behavioral and synaptic actions of psilocybin are independent of 5-HT2R activation in mice. *Proc. Natl. Acad. Sci. USA* **118**, https://doi.org/10.1073/pnas.2022489118 (2021).
46. Sekssaoui, M., Bockaert, J., Marin, P. & Bécamel, C. Antidepressant-like effects of psychedelics in a chronic despair mouse model: is the 5-HT2A receptor the unique player? *Neuropsychopharmacology* **49**, 747–756 (2024).
47. Arnsten, A. F. Stress signalling pathways that impair prefrontal cortex structure and function. *Nat. Rev. Neurosci.* **10**, 410–422 (2009).
48. Li, F. et al. Mediodorsal thalamus projection to medial prefrontal cortical mediates social defeat stress-induced depression-like behaviors. *Neuropsychopharmacology* https://doi.org/10.1038/s41386-024-01829-y (2024).
49. Behlendorf, C. et al. Formation of the pyruvoyl-dependent proline reductase Prd from Clostridioides difficile requires the maturation enzyme PrdH. *PNAS Nexus* **3**, pgae249 (2024).
50. Trip, H., Mulder, N. L., Rattray, F. P. & Lolkema, J. S. HdcB, a novel enzyme catalysing maturation of pyruvoyl-dependent histidine decarboxylase. *Mol. Microbiol.* **79**, 861–871 (2011).
51. Nozaki, S., Webb, M. E. & Niki, H. An activator for pyruvoyl-dependent l-aspartate alpha-decarboxylase is conserved in a small group of the gamma-proteobacteria including Escherichia coli. *MicrobiologyOpen* **1**, 298–310 (2012).
52. Hedstrom, L. Serine protease mechanism and specificity. *Chem. Rev.* **102**, 4501–4524 (2002).
53. Ekici, O. D., Paetzel, M. & Dalbey, R. E. Unconventional serine proteases: variations on the catalytic Ser/His/Asp triad configuration. *Protein Sci.* **17**, 2023–2037 (2008).
54. Krissinel, E. Stock-based detection of protein oligomeric states in jsPISA. *Nucleic acids Res.* **43**, W314–W319 (2015).
55. Torrens-Spence, M. P., Liu, C. T., Pluskal, T., Chung, Y. K. & Weng, J. K. Monoamine biosynthesis via a noncanonical calcium-activatable aromatic amino acid decarboxylase in psilocybin mushroom. *ACS Chem. Biol.* **13**, 3343–3353 (2018).
56. Blei, F. et al. Simultaneous production of psilocybin and a cocktail of beta-carboline monoamine oxidase inhibitors in “magic” mushrooms. *Chemistry* **26**, 729–734 (2020).

57. Yerubandi, A. et al. Acute adverse effects of therapeutic doses of psilocybin: a systematic review and meta-analysis. *JAMA Netw. Open* **7**, e245960 (2024).
58. Harari, R., Chatterjee, I., Getselter, D. & Elliott, E. Psilocybin induces acute anxiety and changes in amygdalar phosphopeptides independently from the 5-HT2A receptor. *iScience* **27**, 109686 (2024).
59. Rakoczy, R. J. et al. Pharmacological and behavioural effects of tryptamines present in psilocybin-containing mushrooms. *Br. J. Pharmacol.* **181**, 3627–3641 (2024).
60. Hibicke, M., Landry, A. N., Kramer, H. M., Talman, Z. K. & Nichols, C. D. Psychedelics, but not ketamine, produce persistent antidepressant-like effects in a rodent experimental system for the study of depression. *ACS Chem. Neurosci.* **11**, 864–871 (2020).
61. Takaba, R. et al. Ethopharmacological evaluation of antidepressant-like effect of serotonergic psychedelics in C57BL/6J male mice. *Naunyn Schmiedebergs Arch. Pharmacol.* **397**, 3019–3035 (2024).
62. Cameron, L. P. et al. 5-HT2ARs mediate therapeutic behavioral effects of psychedelic tryptamines. *ACS Chem. Neurosci.* **14**, 351–358 (2023).
63. Shao, L. X. et al. Psilocybin induces rapid and persistent growth of dendritic spines in frontal cortex in vivo. *Neuron* **109**, 2535–2544 e2534 (2021).
64. Kolasa, M. et al. Unraveling psilocybin's therapeutic potential: behavioral and neuroplasticity insights in Wistar-Kyoto and Wistar male rat models of treatment-resistant depression. *Psychopharmacology* https://doi.org/10.1007/s00213-024-06644-3 (2024).
65. Jefsen, O. et al. Psilocybin lacks antidepressant-like effect in the Flinders Sensitive Line rat. *Acta Neuropsychiatr.* **31**, 213–219 (2019).
66. Farinha-Ferreira, M., Miranda-Lourenco, C., Galipeau, C., Lenkei, Z. & Sebastiao, A. M. Concurrent stress modulates the acute and post-acute effects of psilocybin in a sex-dependent manner. *Neuropharmacology* 110280. https://doi.org/10.1016/j.neuropharm.2024.110280 (2024).
67. Kabsch, W. Xds. *Acta Crystallogr. Sect. D Biol. Crystallogr.* **66**, 125–132 (2010).
68. Emsley, P. & Cowtan, K. Coot: model-building tools for molecular graphics. *Acta Crystallogr. Sect. D Biol. Crystallogr.* **60**, 2126–2132 (2004).
69. Liebschner, D. et al. Macromolecular structure determination using X-rays, neutrons and electrons: recent developments in Phenix. *Acta Crystallogr. D Struct. Biol.* **75**, 861–877 (2019).
70. McCoy, A. J. et al. Phaser crystallographic software. *J. Appl. Crystallogr.* **40**, 658–674 (2007).
71. Murshudov, G. N. et al. REFMAC5 for the refinement of macromolecular crystal structures. *Acta Crystallogr. Sect. D Biol. Crystallogr.* **67**, 355–367 (2011).
72. Perez-Riverol, Y. et al. The PRIDE database at 20 years: 2025 update. *Nucleic acids Res.* **53**, D543–D553 (2025).

Acknowledgements

We thank the staff from BL17B/BL18U1/BL19U1 beamline of the National Facility for Protein Science in Shanghai (NFPS) at Shanghai Synchrotron Radiation Facility for assistance during data collection. We thank the animal facility and the core facility of the Zhongshan School of Medicine, Sun Yat-Sen University. We thank Yubai Zhao for the technical support of immunofluorescence staining. This work was supported by grants from the National Natural Science Foundation of China (31900435 to B.W., 81972967 to W.-J.L., 82272312 to H.C.) and the Guangdong Science and Technology Department (2023B1212060013 and 2020B1212030004 to B.W. and W.-J.L). Fundamental Research Funds for the Central Universities, Sun Yat-Sen University (2023KYPT11 to B.W.). The 100 Top Talent Programs of Sun Yat-Sen University (58000-12230029 to H.C.), and the Shenzhen-Hong Kong-Macao Science and Technology Project (Category C project) (SGDX20220530111403024, H.C.). Mass spectrometry analysis was performed by the Bioinformatics and Omics Center, Sun Yat-Sen Memorial Hospital, Sun Yat-Sen University.

Author contributions

B.W., H.C., Y.Q., and W.-J.L. conceived the project. C.M., W.G., and Y.W. expressed, purified, and grew the crystals. W.G., X.Z., Y.L., H.L., Q.Z., S.X., Y.Q., and C.M. performed the biochemical assays. W.G. and Y.W. collected X-ray diffraction data. C.X. performed the behavior experiments. B.W., H.C., S.X., and W.-J.L. solved and interpreted the structures and experimental data. B.W., H.C., Y.Q., and W.-J.L. wrote and revised the manuscript. B.W. supervised the structural and biochemical studies. W.-J.L. supervised the in vivo experiments.

Competing interests

The authors declare no competing interests.

Additional information

Supplementary information The online version contains supplementary material available at https://doi.org/10.1038/s41467-025-58239-x.

Correspondence and requests for materials should be addressed to Yuntan Qiu, Haitao Chen, Wei-Jye Lin or Baixing Wu.

Peer review information *Nature Communications* thanks Wulf Blankenfeldt, Roberto Steiner, and the other, anonymous, reviewers for their contribution to the peer review of this work. A peer review file is available.